Characterizing M/EEG measures of pain through biophysically-principled neuromodeling and spectral event analysis

By

Ryan V. Thorpe

B.S., Walla Walla University, 2016

Thesis

Submitted in partial fulfillment of the requirements for the Degree of Master of Science in the School of Engineering and Center for Biomedical Engineering at Brown University

PROVIDENCE, RHODE ISLAND

MAY 2019

AUTHORIZATION TO LEND AND REPRODUCE THE THESIS

As the sole author of this thesis, I authorize Brown University to lend it to other institutions or individuals for the purpose of scholarly research.

Date_____ _____

Ryan V. Thorpe, Author

I further authorize Brown University to reproduce this thesis by photocopying or other means, in total or in part, at the request of other institutions or individuals for the purpose of scholarly research.

Date_____ _____

Ryan V. Thorpe, Author

This thesis by Ryan V. Thorpe is accepted in its present form by the School of Engineering and the Center for Biomedical Engineering as satisfying the thesis requirements for the degree of Master of Science.

Date_____ _____

David A. Borton, Advisor

Date_____ _____

Stephanie R. Jones, Co-advisor

Date_____ _____

Carl Y. Saab, Co-advisor

Approved by the Graduate Council

Date_____ _____

Andrew G. Campbell, Dean of the Graduate School

Acknowledgments

Throughout my time at Brown University, Professors David Borton, Stephanie Jones, and Carl Saab have provided steadfast support for both myself and this project. I am incredibly grateful for everything they have taught me; without their expertise, mentorship, and encouragement, none of this would have been possible.

My colleagues in the Borton, Jones, and Saab labs have also played a crucial role in broadening my perspectives, troubleshooting problems, and inspiring me daily to pursue research despite its hurdles. In particular, I want to thank Josh Levitt who has worked closely with me in processing the Lumbar Radiculopathy EEG dataset, Chris Black and Hyeyoung Shin for numerous insightful discussions regarding experimental approach and analysis techniques, and Sam Neymotin and Blake Caldwell for their help implementing Human Neocortical Neurosolver (HNN) with its various computational needs. HNN simulations were conducted using the OSCAR computing cluster at the Center for Computation and Visualization, Brown University.

As part of a larger study facilitated by the Saab lab, collection of the Lumbar Radiculopathy EEG dataset was funded by Asahi Kasei Pharma, Japan and conducted by Dr. Muhammad Edhi under Dr. Alexios Carayannopoulos of Rhode Island Hospital's Comprehensive Spine Center.

Two other datasets referenced in this study were provided by Cédric Lenoir [1] and Li Hu [2], respectively. I am particularly grateful for their correspondence and willingness to collaborate.

Most importantly, I would like to thank my family. My mom, Elizabeth, and wife, Kelsey, in particular have always supported my reckless pursuit of science. I can confidently say that any degree of success on my part only dimly reflects the articulate passion these two women put into everything they do.

Contents

Acknowledgments **iii**

Contents **v**

List of Figures **xi**

Abstract **1**

Introduction **3**

1 Biophyisically-principled neuromodeling of the early-latency, nociceptive evoked M/EEG response in S1 **5**

1.1 Background 5

1.2 Testing circuit mechanisms with HNN 12

1.2.1 Early-latency MNEP emerges from sequential proximal and distal drive events 13

1.2.2 Early-latency LEP emerges from phase-locked bursts of proximal and distal drive 16

1.3 Discussion 18

2 Spectral event analysis in resting-state chronic pain EEG **22**

2.1 Background 22

2.2 Materials and Methods 23

2.2.1 Human EEG trials 23

2.2.2 Preprocessing and epoch selection 24

2.2.3 Identifying frequency bands of interest 24

2.2.4 Spectral event detection and feature comparison 25

2.3 Results 28
2.3.1 Only one frequency band near 40 Hz and over somatosensory cortex separates spontaneous EEG activity in LR versus healthy subjects 28
2.3.2 The LR group exhibits 40 Hz spectral events at a different rate and with a different frequency-span compared to the healthy group 33
2.4 Discussion 35

Conclusion **38**

List of Figures

1.1 Equivalent current dipole (ECD) location (area 3b/1) and orientation of the Aβ-N20 (from contralateral median nerve stimulation) and Aδ-N1 (from contralateral laser stimulation). Both images represent ECD activation within the left hemisphere due to right-hand stimulation, oriented upward/anterior (left) and downward/posterior (right). For the image corresponding to median nerve stimulation (left), note that the axial plane is flipped about the medial axis. Adapted from Kanno et al. (2003), Fig. 3 [29] and Jin et al. (2018), Fig. 3 [2]. 6

1.2 Reconstruction of a layer 5 pyramidal neuron from the rat somatosensory cortex. Stereotypical morphology includes the soma, basal dendrites that extend minimally from the base of the soma in many directions, apical dendrites (among which is a long distal dendrite) that extend upward from the apex, and an axon that projects from the bottom of the soma (not shown). Adapted from Chen et al. (2003), Fig. 6 [39]. 7

1.3 Evoked response to median nerve stimulation with its stereotypical primary deflections, N20 and P35, across different experimental paradigms and data sources. Blue: ECD, originally in units of dSPM, is extracted from an image supplied by Alexandre Gramfort [40]; orange: ECD, originally in units of nAm, is extracted from Figure 2 in Lin et al. (2003) [36]; yellow: ECD, originally in units of nAm, is computed from the MNE-Python somatosensory dataset [40, 41]; and purple: EEG Cc-Fz is read directly from the dataset in Lenoir et al. (2017) [1]. Each waveform is rescaled to orient the N20 deflection upward with a total waveform euclidean norm of 1. Note that the blue, orange, and yellow waveforms represent estimated source-space dipoles, while the purple waveform represents the EEG sensor-space ERP measured at the C3 and C4 electrodes (contralateral to stimulation) referenced at Fz. 8

1.4 Forward-solution waveforms of different dipoles calculated with the assumption that the MNEP N20 and P35 deflections are better explained by two separate sources. The top waveform corresponds to the N20 ECD, the middle waveform corresponds to the P35 ECD, and the bottom plot represents the goodness-of-fit for the N20 source alone (dotted line) and the combination of the two sources (solid line). The left and right sides denote experimental paradigms where median nerve stimulation is applied with a 5 s and 1 s inter-stimulus-interval, respectively. Adapted from Wikstrom et al. (1996), Fig. 5 [35]. 10

1.5 Mechanistic origin of the electromagnetic fields measured by M/EEG. Primary currents traveling down the distal dendrites of pyramidal neurons in the neocortex produce a net dipole, which in turn creates an electromagnetic field. Reproduced from the *Encyclopedia of Computational Neuroscience* [42]. 11

1.6 Schematic of the laminar HNN model. Each vertical section of a 10x10 grid contains a layer 2/3 (L2/3) pyramidal cell (at the upper plane) and a layer 5 (L5) pyramidal cell (at the lower plane). Additionally, 35 inhibitory basket cells per layer are distributed among the pyramidal cells in conjunction with a series of local and excitatory input (proximal and distal drive) connections. 13

1.7 Simulation of the Aβ-N20 complex. This simulation is conducted with 100 trials (grey) to form the trial average (black) and compared via root mean squared error (RMSE) to the experimentally observed ECD (purple). A proximal (red) input occurs at t = 20 ms and two distal (green) inputs occured at t = 32 and 82 ms. The top plots denote time histograms corresponding to each input. 14

1.8 Spiking of the simulated dipoles of the Aβ-N20 complex. Top: time histograms of distal (green) and proximal (red) inputs, middle: raster plot of individual cell spiking (organized by cell-type), and bottom: time histograms corresponding to the combined spiking of all cells per cell type. 15

1.9 Layer-specific simulated current dipoles of the Aβ-N20 complex. 16

1.10 Simulations of the Aδ-N1 complex at four stages. All simulations are conducted with 100 trials (grey) to form the trial average (black) and compared via root mean squared error (RMSE) to the experimentally observed ECD (purple). Proximal (red) and distal (green) inputs are assigned successively as follows: a) add three proximal inputs at t = 120, 145, and 170 ms; b) add one distal input at t = 145 ms; c) add a three-spike burst of distal inputs 25 ms apart, starting at t = 120 ms; and d) adjust the last distal input to occur earlier at t = 195 ms. The top plots denote time histograms corresponding to each input. Note that the same local network and cellular parameters determined for the modeled Aβ-N20 complex ECD are used here. 17

1.11 Decreased Aδ-N1 complex matching due to deviations in the input timing at stage 4. Starting off at the model simulation shown in stage 4 (Figure 1.10.d) (a), decreasing the proximal presynaptic ISI from 125 ms to 100 ms renders an average RMSE of 8.33 (b). On the other hand, increasing the distal presynaptic ISI from 25 ms to 35 ms renders an average RMSE of 8.84 (c). 18

1.12 Traditional understanding of the circuit mechanisms behind the MNEP: a) excitatory drive from lemniscal thalamus enters the granular layer of area 3b, resulting in an initial depolarizing current being driven up the distal dendrites from the soma of the pyramidal cells, b) after a small time delay, inhibitory drive from activated basket cells reaches the pyramidal cell's soma, causing a net downward flow of current, a secondary excitatory drive excites the soma of the pyramidal cells and once again drive current up the distal dendrites, and d) secondary activation of the basket cells results in more inhibitory drive to the soma of pyramidal cells, resulting in another downward net current. Reproduced from Wikstrom et al. (1996), Fig. 6 [35]. 19

2.1 Spectral event detection in ten sample epochs for the 18th LR subject, eyes open. The top spectrogram displays the average TFR over all epochs. The ten bottom spectrograms display randomly sampled, single-epoch TFRs with their corresponding waveforms. Note that the ten bottom spectrograms only show activity in the frequency band of interest (42-43 Hz) and the left and right sides show the same TFR before and after median-PSD normalization, respectively. White dots correspond to the time-frequency coordinates of isolated spectral events calculated from the median-normalized TFR. 27

2.2 Characteristic median-normalized time-frequency domain activity for channel C3 (eyes open), compared between the LR versus healthy groups. The group average (a-b) is averaged across all subject-specific average TFRs (c-d). In (e-g), maroon corresponds with the LR group median and black corresponds with the healthy group median. In (g), the orange region (42-43 Hz) indicates statistically significant PSD differences between the two groups (two-tailed Wilcoxon rank sum test corrected for multiple comparisons at 0.05 significance, $p < 0.0011$). Confidence intervals are computed using a 10,000 iteration bootstrap procedure. 29

2.3 Median-normalized PSDs for all channels besides C3 (eyes open), compared between the LR versus healthy groups. Maroon corresponds with the LR group median and black corresponds with the healthy group median. No frequency values for channels CZ (a), F8 (b), FP1 (c), and FP2 (d) contain statistically significant PSD differences between the two groups (two-tailed Wilcoxon rank sum test corrected for multiple comparisons at 0.05 significance, $p > 0.0011$). Confidence intervals are computed using a 10,000 iteration bootstrap procedure. 30

2.4 Characteristic median-normalized time-frequency domain activity for channel C3 (eyes closed), compared between the LR versus healthy groups. The group average (a-b) is averaged across all subject-specific average TFRs (c-d). In (e-g), maroon corresponds with the LR group median and black corresponds with the healthy group median. In (g), the orange region (38-43 Hz) indicates statistically significant PSD differences between the two group (Wilcoxon rank sum test corrected for multiple comparisons at 0.05 significance, $p < 0.0011$). Confidence intervals are computed using a 10,000 iteration bootstrap procedure. 31

2.5 Median-normalized PSDs for all channels besides C3 (eyes closed), compared between the LR versus healthy groups. Maroon corresponds with the LR group median and black corresponds with the healthy group median. No frequency values for channels CZ (a), F8 (b), FP1 (c), and FP2 (d) contain statistically significant PSD differences between the two groups (Wilcoxon rank sum test corrected for multiple comparisons at 0.05 significance, $p > 0.0011$). Confidence intervals are computed using a 10,000 iteration bootstrap procedure. 32

2.6 Probability histograms of spectral event features (counts/epoch, power, duration, and frequency span) in the 42-43 Hz range for channel C3, eyes open. From left to right: LR subjects, healthy controls, and subject aggregates from the respective groups. Maroon denotes the aggregate histogram for LR and black denotes the aggregate histogram for healthy subjects. *statistically significant difference between the aggregate feature distribution of the LR group compared to the healthy group (Wilcoxon rank sum test corrected for multiple comparisons at 0.01 significance, $p < 0.0025$). 34

2.7 Probability histograms of spectral event features (counts/epoch, power, duration, and frequency span) in the 38-43 Hz range for channel C3, eyes closed. From left to right: LR subjects, healthy controls, and subject aggregates from the respective groups. Maroon denotes the aggregate histogram for LR subjects and black denotes the aggregate histogram for healthy subjects. *statistically significant difference between the aggregate feature distribution of the LR group compared to the healthy group (Wilcoxon rank sum test corrected for multiple comparisons at 0.01 significance, $p < 0.0025$). 35

Abstract

Numerous neural imaging and electrophysiological markers have been identified as correlates of pain, however, none have provided for the reliable, quantitative measurement of a human's perceptual experience. In order to construct a more principled understanding of the cortical signals indicative of acute and chronic pain, this study takes two approaches, respectively. Part 1 elucidates where, when, and how noxious sensory input translates into magneto- and electroencephalography (M/EEG) evoked responses in primary somatosensory cortex (S1). Specifically, Part 1 uses a biophysically-principled model of a cortical column, Human Neocortical Neurosolver (HNN), to simulate the circuit mechanisms underlying the early-latency laser-evoked potential (LEP) versus median nerve stimulation-evoked potential (MNEP). The HNN model demonstrates that the early-latency LEP (i.e., the Aδ-N1 complex) emerges from S1 as the unique result of a phase-locked burst of proximal drive (from lemniscal thalamus to S1 layer 4) and distal drive (from high-order cortex or non-lemniscal thalamus to S1 layer 2/3). Furthermore, the inter-spike interval of pre-synaptic inputs occur at a theta period (125 ms) and gamma period (25 ms), respectively. Part 2 examines the transient nature of spectral EEG activity in humans with resting-state chronic pain (i.e., lumbar radiculopathy). Motivated by the understanding that governing mechanisms of "rhythmic" neural activity begin and end in finite time, Part 2 compares four features of spectral events (i.e., count/epoch, power, duration, and frequency span) between the chronic pain and healthy control populations in empirically-determined frequency bands. Centered around 40 Hz, spectral event analysis revealed that three of the four features (count/epoch, peak power, and frequency span) were significantly different between the two populations for the eyes open condition and two of the four features (count/epoch and frequency span) where significantly different between the two populations for the eyes closed condition. Overall, the results of this study predict that specific bursts of

rhythmic events facilitate transfer of pain-related information and call for a more targeted investigation for their use as both biomarkers and underlying circuit mechanisms.

Introduction

In the U.S. alone, an estimated 11.3% of the population reports experiencing chronic or high levels of pain on a regular basis [3]. Despite the obvious need for targeted neuropathic pain therapies, most treatments rely on one-size-fits-all approaches with limited efficacy and numerous negative side effects. Mainstream oral medications (e.g., oxycontin), for instance, are assigned in prototypical dosages, and often derive from highly addictive substances. In uncontrolled settings, such medications have contributed to large-scale abuse (and even death) in what has become a national opioid crisis. Spinal cord stimulation (SCS) presents an attractive alternative, though it requires invasive surgery, operates in a mostly open-loop paradigm, and correspondingly reports varying levels of efficacy [4, 5]. Only with considerable effort and over multiple appointments can a clinician hope to achieve an adequate stimulation configuration that reduces excessive pain and increases patient mobility. To open the door for more effective therapies, researchers have called for a more principled search for pain "biomarkers" that 1) allow for increased pain classification accuracy and 2) provide functional understanding to underlying neural circuitry for targeted modulation of pain-related information [6–8].

The search for reliable, physiologically-relevant measures of pain is no simple task: pain processing integrates across the cognitive, emotional, and sensory dimensions of neural activity [6, 9–11], as well as numerous physical locations in the brain forming what has become known as the "pain matrix" [6, 10–14]. The pain matrix is typically thought to include the thalamus, primary (S1) and secondary (S2) somatosensory cortices, anterior cingulate cortex (ACC), prefrontal cortex (PFC), and insula, however, the relative involvement of these areas remains poorly understood and might, indeed, include other brain structures like the cerebellum [15]. Furthermore, certain prolifically used imaging modalities like functional magnetic resonance imaging (fMRI) rely on indirect measures of brain activity and lack millisecond-scale precision [6]. The blood-

oxygen-level-dependent (BOLD) signal measured by fMRI cannot account for spiking or inter-neuron circuit dynamics and its limited precision in the time domain causes significant blurring in the spatial domain due to fast timescale activation of different brain regions. A similar limitation emerges for time and frequency-domain analysis (regardless of the modality) that only considers average responses across time or trials: spontaneous processes that govern context dependency via a resting brain state get washed out or misinterpreted [16, 17]. Therefore, the shortcomings of traditional approaches for finding and interpreting pain biomarkers (e.g., solving for sequential activation of pain matrix regions via fMRI or isolating shifts in the peaks of average spectral power [18–20]) can be mitigated by leveraging methods that translate between sensor and neural circuit, have millisecond-scale precision, and address spontaneous events in single-time-series resting state activity.

This study takes two separate paths in order to predict events in magneto- and electroencephalography (M/EEG) measures of acute and chronic pain, respectively, that contain circuit-level significance. Under the hypothesis that the underlying circuit mechanisms of the evoked acute pain M/EEG response differ from those of non-painful sensory stimuli, Part 1 runs simulations on a computational biophysically-principled model, Human Neocortical Neurosolver (HNN), of the primary neuronal activity responsible for M/EEG signals [21–23]. As discussed more in Section 1.2, HNN exhibits laminar and morphological structure, two classes of inputs simulating "feedforward" and "feedback" drive, and excitatory and inhibitory connections that preserve the functional significance of neocortical neuronal circuits. Upon accurate simulation of experimentally observed evoked responses, the synaptic input parameters represent precisely timed circuit perturbations that encode transmission of nociceptive information to the neocortex. Part 2, on the other hand, identifies transient spectral events that arise spontaneously in resting state EEG of chronic pain versus normal human subjects. Thus, Part 2 addresses the confounding influence of chronic pain on stochastic brain states under the hypothesis that the number, magnitude, and breadth of high-power spectral events account for a substantial change from healthy resting state activity.

Part 1

Biophyisically-principled neuromodeling of the early-latency, nociceptive evoked M/EEG response in S1

1.1 Background

Nociceptive stimulus to the hand evokes its earliest M/EEG response in contralateral S1 [2, 24, 25], specifically area 3b/1 [26–28]. As reflected in Figure 1.1, non-nociceptive median nerve stimulation [29–37] (and more broadly tactile hand stimulation [21, 31]) evokes an initial response in a topologically similar region of contralateral S1. Although most previous studies have analyzed the nociceptive and non-nociceptive sensory early-latency evoked responses separately, here we consider the cortical circuit mechanisms underlying each waveform in relation to the other. Specifically, we consider the circuit-level origin of the early-latency laser evoked potential (LEP) Aδ-N1 complex, originating from cutaneous laser stimulation to the hand and transmitted primarily through Aδ fibers [2, 26, 27], in reference to the median nerve evoked potential (MNEP) Aβ-N20 complex, originating from transcutaneous electrical median nerve stimulation and transmitted primarily through Aβ fibers [38].

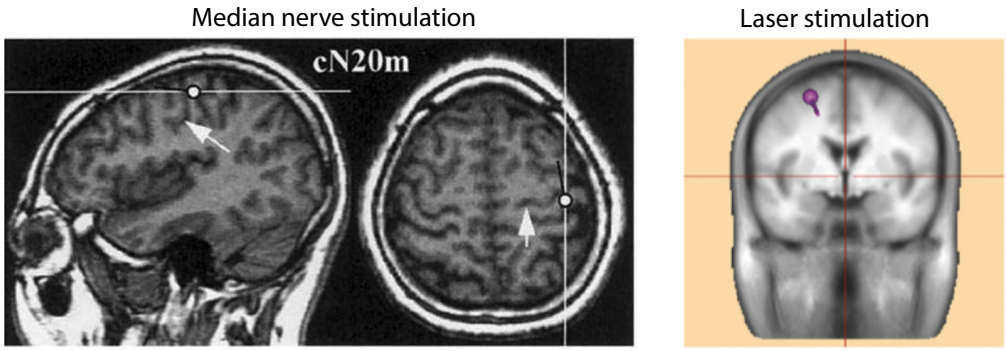

Figure 1.1. Equivalent current dipole (ECD) location (area 3b/1) and orientation of the Aβ-N20 (from contralateral median nerve stimulation) and Aδ-N1 (from contralateral laser stimulation). Both images represent ECD activation within the left hemisphere due to right-hand stimulation, oriented upward/anterior (left) and downward/posterior (right). For the image corresponding to median nerve stimulation (left), note that the axial plane is flipped about the medial axis. Adapted from Kanno et al. (2003), Fig. 3 [29] and Jin et al. (2018), Fig. 3 [2].

Given that both the Aβ-N20 complex and Aδ-N1 complex source-localize to locations on the posterior wall of the central sulcus, we characterize each waveform by first considering the orientation of their respective equivalent current dipoles (ECDs). The initial N20 deflection of the Aβ-N20 complex ECD points upward with reference to the surface of the cortex and indicates electrical current flow up toward the surface of the cortex [35]. Conversely, the initial N1 deflection of the Aδ-N1 complex ECD points downward and indicates electrical current flow down from the surface of the cortex. (As discussed in more detail later, bulk current flow in the cortex primarily travels through the long distal dendrites of pyramidal neurons that span multiple layers of the cortex. Since distal dendrites extend normal to the surface of the cortex as in Figure 1.2, they are generally oriented parallel to each other and thus contribute the most to net current flow within a cortical column.)

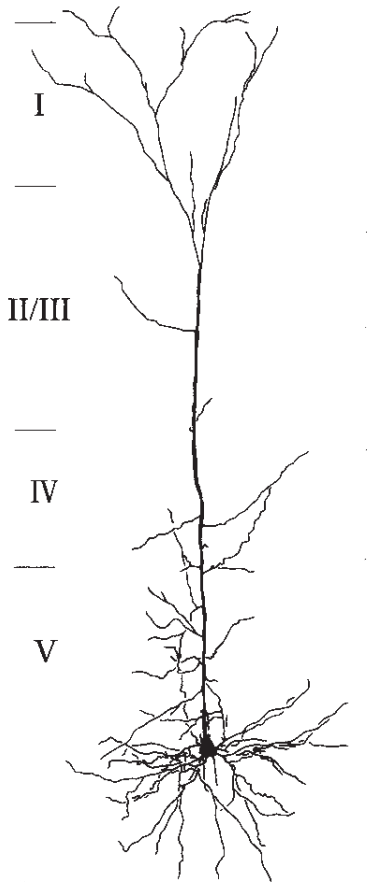

Figure 1.2. Reconstruction of a layer 5 pyramidal neuron from the rat somatosensory cortex. Stereotypical morphology includes the soma, basal dendrites that extend minimally from the base of the soma in many directions, apical dendrites (among which is a long distal dendrite) that extend upward from the apex, and an axon that projects from the bottom of the soma (not shown). Adapted from Chen et al. (2003), Fig. 6 [39].

While the ECD orientation of the Aδ-N1 in Figure 1.1 appears to differ slightly from that of the Aβ-N20, nociceptive projections to S1 are known to activate populations closer to the crown of the post-central gyrus (i.e., occupying a topological region between areas 3b and 1) [27, 28]. Such a location supports a more downward-pointing ECD orientation in order to remain normal to the brain's surface. With this in mind, now consider the stereotypical early-latency Aβ-N20 complex shown in 1.3. The waveform exhibits two primary deflections, upward then downward, followed by a congruent (but last drastic) secondary pattern. While the exact timing of the N20 and P35 deflections possesses a certain amount of inter-population and inter-experimental variability, the relative progression of a small upwards deflection followed by a considerably larger

downward deflection appears ubiquitous throughout the literature [1, 29–37].

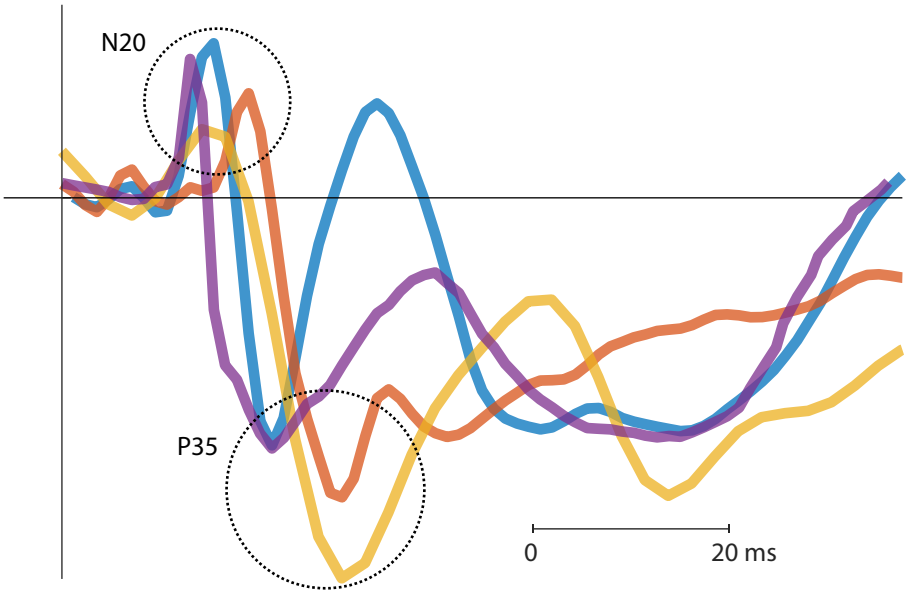

Figure 1.3. Evoked response to median nerve stimulation with its stereotypical primary deflections, N20 and P35, across different experimental paradigms and data sources. Blue: ECD, originally in units of dSPM, is extracted from an image supplied by Alexandre Gramfort [40]; orange: ECD, originally in units of nAm, is extracted from Figure 2 in Lin et al. (2003) [36]; yellow: ECD, originally in units of nAm, is computed from the MNE-Python somatosensory dataset [40, 41]; and purple: EEG Cc-Fz is read directly from the dataset in Lenoir et al. (2017) [1]. Each waveform is rescaled to orient the N20 deflection upward with a total waveform euclidean norm of 1. Note that the blue, orange, and yellow waveforms represent estimated source-space dipoles, while the purple waveform represents the EEG sensor-space ERP measured at the C3 and C4 electrodes (contralateral to stimulation) referenced at Fz.

It is important to note here that we draw a distinction between the ECD of the early-latency MNEP and the ECD of the Aβ-N20. Since any given sensor-space waveform can emerge from multiple ECDs, the ECD that contributes the most to a given sensor-space *deflection* (e.g., Aβ-N20) is not necessarily the same as the ECD that contributes the most to the response's entire waveform (e.g., the successive N20, P35, etc. deflections that together compose S1's evoked response to contralateral median nerve stimulation). Numerous researchers have demonstrated that the neural generators of the

Aβ-N20 and Aβ-P35, respectively, may be distinct [30, 33–35]. For example, Wikstrom et al. demonstrated that multi-dipole modeling extracts two noticeably different ECDs corresponding to different deflections in the MNEP (Figure 1.4) [35]. Furthermore, Wikstrom et al. showed that 1) a multi-source model outperforms a single-source N20 model in goodness-of-fit when reproducing the forward-solution and 2) the respective N20 and P35 ECDs have functionally different responses to modulation of the median nerve inter-stimulus-interval. Therefore, any single ECD identified as "most characteristic" of the early-latency MNEP may in practice correspond to either (or a combination) of the two major sensor-space deflections, N20 and P35, depending on the optimization routine. A similar distinction applies to any reference in the following pages to the ECD of the early-latency LEP (i.e., Aδ-N1 *complex*) versus the ECD of the Aδ-N1 *deflection*.

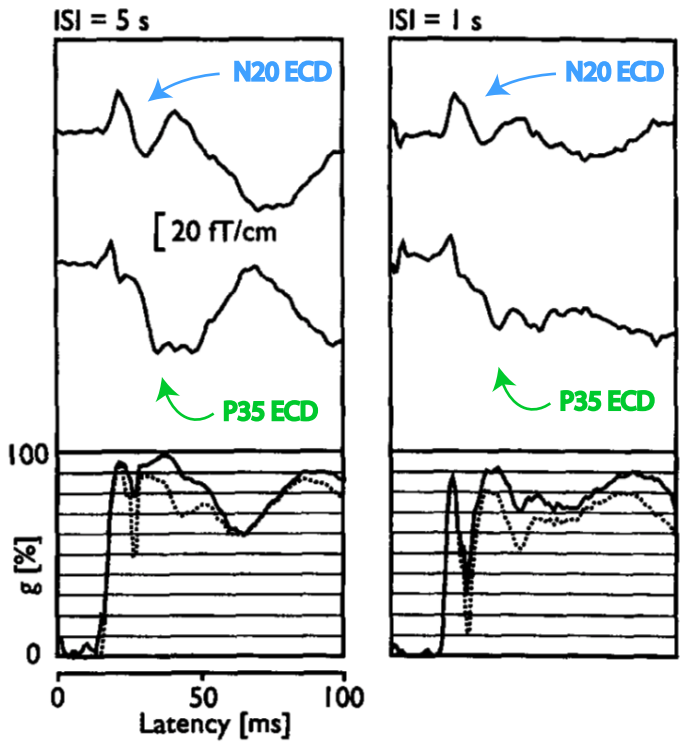

Figure 1.4. Forward-solution waveforms of different dipoles calculated with the assumption that the MNEP N20 and P35 deflections are better explained by two separate sources. The top waveform corresponds to the N20 ECD, the middle waveform corresponds to the P35 ECD, and the bottom plot represents the goodness-of-fit for the N20 source alone (dotted line) and the combination of the two sources (solid line). The left and right sides denote experimental paradigms where median nerve stimulation is applied with a 5 s and 1 s inter-stimulus-interval, respectively. Adapted from Wikstrom et al. (1996), Fig. 5 [35].

Broadly speaking, the ECD of any arbitrary response gives insight into the structure and dynamics of its corresponding neocortical circuit. Dipole location and orientation show the primary direction of current flow through the distal dendrites of cortical pyramidal neurons (Figure 1.5): either ascending from deep layers toward the surface of the brain or descending from superficial layers toward deep layers. Also, timing of ECD peak deflections represent windows of maximal current flow in one direction or the other. Finally, the relative amplitude of one ECD to another (measured as root mean squared error from baseline) scales proportionally with the number of pyramidal neurons that contribute current flow to the combined ECD normal to the surface of the brain.

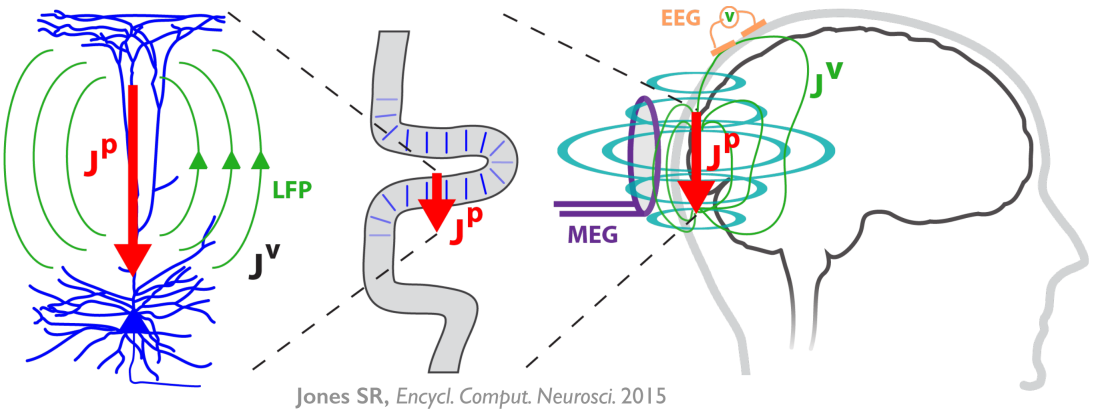

Figure 1.5. Mechanistic origin of the electromagnetic fields measured by M/EEG. Primary currents traveling down the distal dendrites of pyramidal neurons in the neocortex produce a net dipole, which in turn creates an electromagnetic field. Reproduced from the *Encyclopedia of Computational Neuroscience* [42].

Given the observation that the respective ECDs corresponding to the Aδ-N1 complex and Aβ-N20 complex originate from reasonably similar topographic locations and axis orientations, we make two hypotheses regarding the primary underlying dipole circuits of each response.

Hypothesis 1 *The primary underlying circuits responsible for the Aδ-N1 complex and Aβ-N20 complex ECDs, respectively, are functionally congruent. As such, each circuit can account for both responses given the same local network components, local network connectivity, and similar types of inputs (originating from lemniscal thalamus and non-lemniscal thalamus or high-order cortex).*

As a consequence of the first hypothesis, we address the mechanisms significant to nociception more directly in the second:

Hypothesis 2 *A change in the number and timing of inputs adequately accounts for the difference in LEP versus MNEP, thus isolating a circuit mechanism unique to nociception.*

In other words, we expect to find that the early-latency nociceptive evoked response emerges differentially from its non-nociceptive, MNEP control due to specifically timed perturbations of the same S1 circuit. If both hypotheses are true, the input configuration (i.e., number and timing of inputs) form a characteristic mechanism of the nociceptive

evoked response in S1. Such a mechanism can be tested further for in vivo physiological support. On the other hand, if one or both hypotheses prove to be false, we demonstrate that a reduction of the two respective ECD circuits to one circuit is shortsighted. It should be noted here that for the scope of this study, Hypothesis 1 and 2 are not intended to be conclusively accepted or rejected. Rather, they are asserted in order to create a tangible framework that allows for simulation experiments to guide future neurophysiological experiments. Such an approach enables computationally-informed predictions of neural dynamics to be found that would have otherwise been difficult (if not impossible) to find. As addressed further in Part 2 of this study, a corollary of Hypothesis 2 extends to a more general, non-time-locked paradigm by predicting that the number, magnitude, and breadth of high-power spectral events, measured at a given EEG electrode, account for a substantial change from healthy resting state activity.

1.2 Testing circuit mechanisms with HNN

Part 1 of this study employed use of HNN, a biophysically principled model of somatosensory cortex [23], to simulate the current dipole circuits underlying M/EEG (Figure 1.5). More specifically, HNN simulates the primary current flow up and down the distal dendrites of a pyramidal neuron by incorporating it into the model shown in Figure 1.6) [21, 22, 43]. Two classes of synaptic inputs simulate perturbations of the cortical circuit coming from the peripheral nervous system through the lemniscal thalamus (i.e., proximal inputs) or from top-down control through non-lemniscal thalamus or high-order cortex (i.e., distal inputs). Distinguishing between these inputs allows the model to simulate circuit drive that initially pushes current flow up from the soma or pushes current flow down toward the soma from superficial layers. Furthermore, proximal and distal inputs drive inhibitory basket cells at different latencies given the distance and number synaptic connections separating inital activation from each basket cell. While many parameters play a significant role in determining modes of HNN's high-dimensional dynamical system, this study primarily focuses on modulating the type and relative timing of circuit inputs (guided by the hypotheses asserted above).

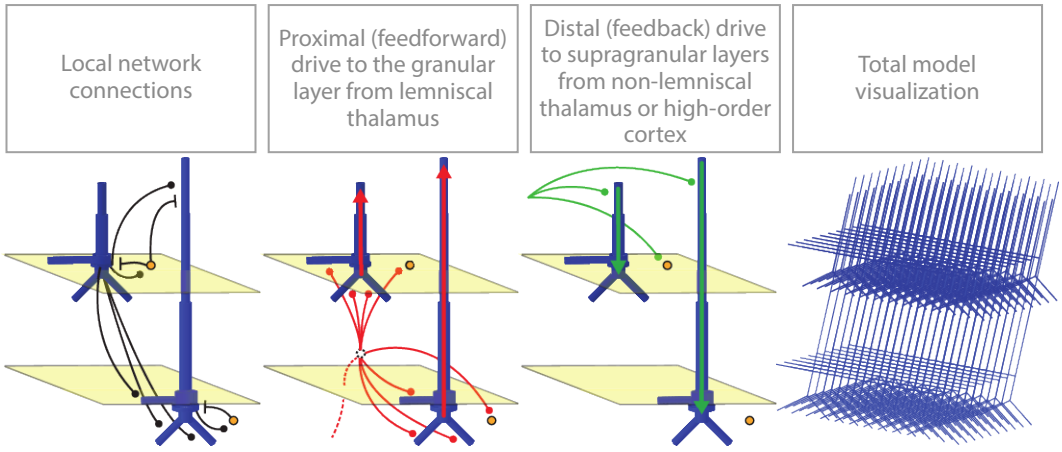

Figure 1.6. Schematic of the laminar HNN model. Each vertical section of a 10x10 grid contains a layer 2/3 (L2/3) pyramidal cell (at the upper plane) and a layer 5 (L5) pyramidal cell (at the lower plane). Additionally, 35 inhibitory basket cells per layer are distributed among the pyramidal cells in conjunction with a series of local and excitatory input (proximal and distal drive) connections.

Prior to running simulations, the median nerve stimulation inverse solution was extracted from MNE-Python somatosensory dataset [40, 41] by solving for the minimum norm estimate [44] and then selecting the vertex that contributed the largest normal component (to the surface of the brain) over the 0-42 ms post-stimulus time window. The resulting waveform (i.e., the yellow trace in Figure 1.3) was used as a reference for HNN simulations of the early-latency MNEP ECD. The LEP ECD waveform was retrieved from Li Hu and represents the group average ECD of contralateral early-latency LEPs isolated through independent component decomposition [2]. See Jin et al. (2018) [2] for specific details regarding experimental procedure and the inverse solution of the Aδ-N1 complex.

1.2.1 Early-latency MNEP emerges from sequential proximal and distal drive events

Solving first for the HNN simulation parameters pertaining to the Aβ-N20 complex, simulations sessions were run iteratively to create the modeled average waveform shown in Figure 1.7. Layer-specific activity (Figure 1.9) and neuron spiking (1.8) were also considered. The model variables associated with the input number, type, timing, and $AMPA$ and $NMDA$ weights for layer-specific pyramidal and basket cells were manually

modified. Furthermore, model variables associated with local connectivity for $AMPA$, $NMDA$, $GABA_A$, and $GABA_B$ weights onto layer-specific pyramidal cells were modified. All simulations for both waveforms were run with a 0.025 ms integration time-step, 100 trials/simulation, and a 5 ms Gaussian smoothing window.

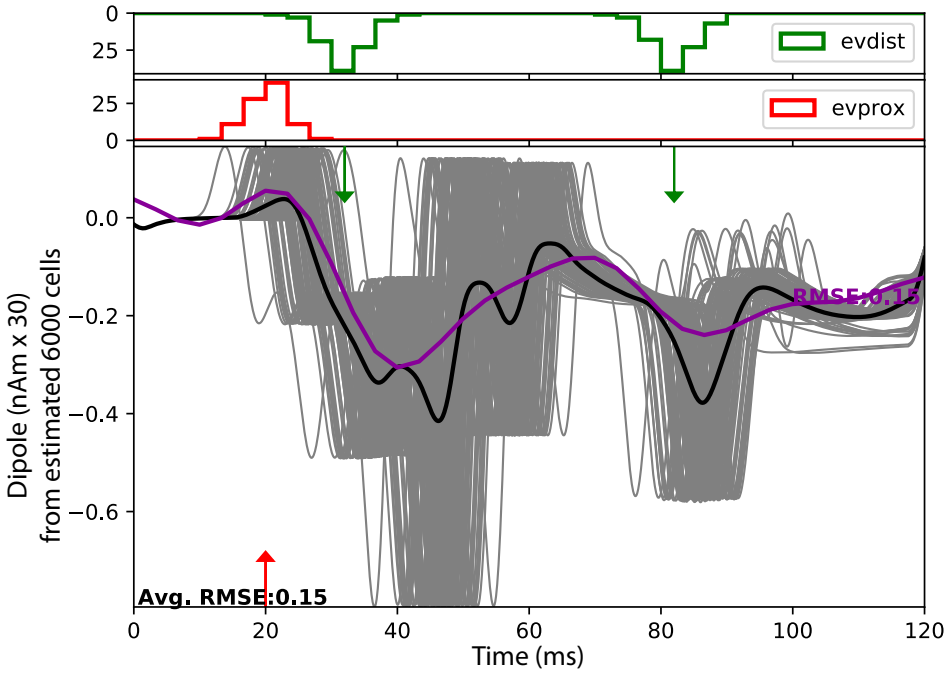

Figure 1.7. Simulation of the Aβ-N20 complex. This simulation is conducted with 100 trials (grey) to form the trial average (black) and compared via root mean squared error (RMSE) to the experimentally observed ECD (purple). A proximal (red) input occurs at t = 20 ms and two distal (green) inputs occured at t = 32 and 82 ms. The top plots denote time histograms corresponding to each input.

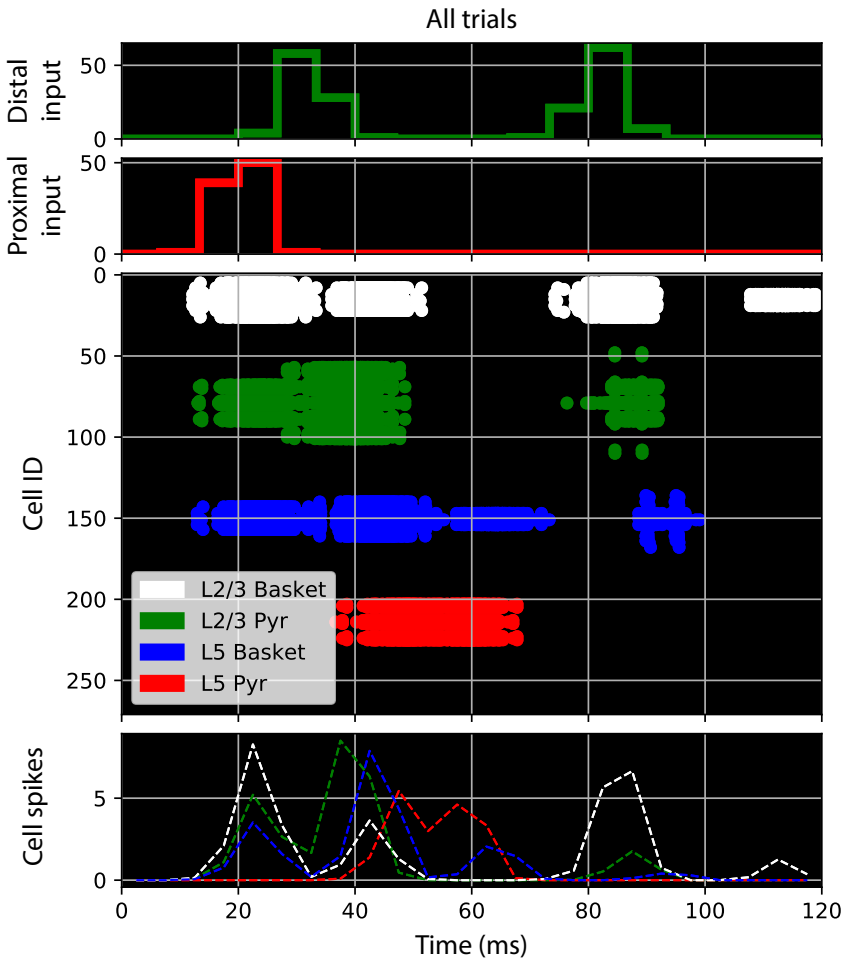

Figure 1.8. Spiking of the simulated dipoles of the Aβ-N20 complex. Top: time histograms of distal (green) and proximal (red) inputs, middle: raster plot of individual cell spiking (organized by cell-type), and bottom: time histograms corresponding to the combined spiking of all cells per cell type.

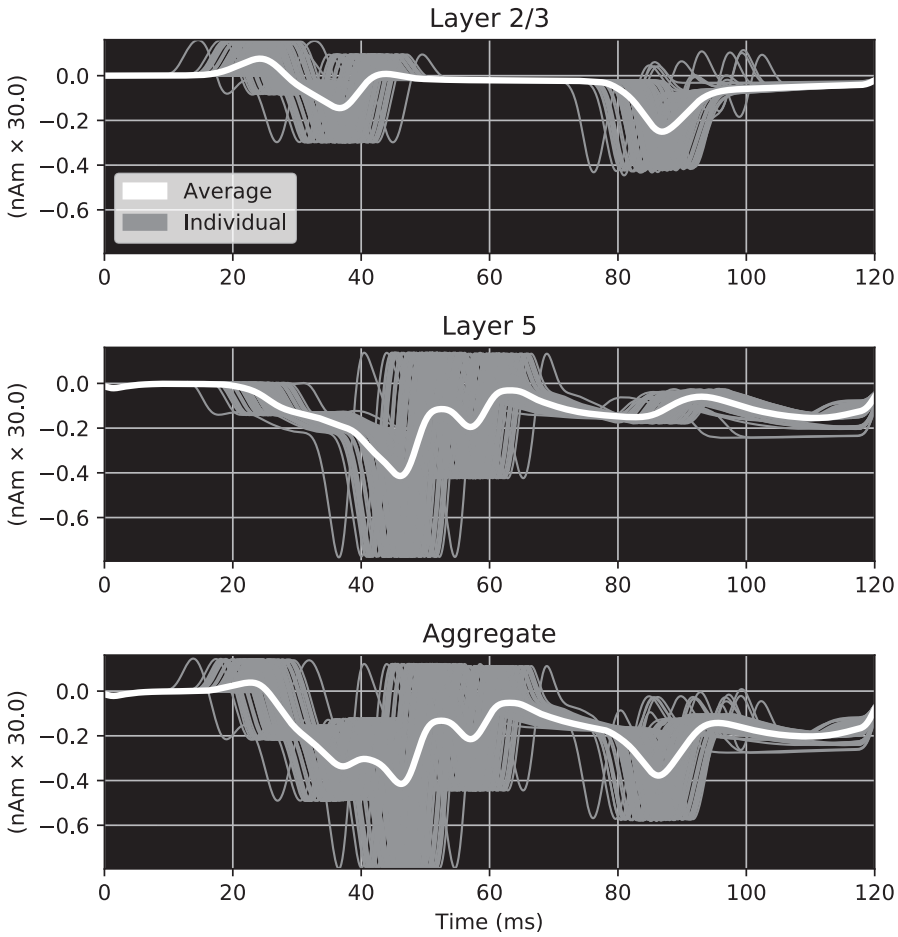

Figure 1.9. Layer-specific simulated current dipoles of the Aβ-N20 complex.

1.2.2 Early-latency LEP emerges from phase-locked bursts of proximal and distal drive

Once the modeled Aβ-N20 complex was articulated, all local connectivity parameters remained constant while adjustments were made to the number, type, and timing of inputs. As shown in Figure 1.10, HNN modeling of the Aδ-N1 complex is best described in four stages. Each stage corresponds to an informed modification of the simulation inputs that attempts to account for most prominent temporal features first, followed by less prominent. Arriving at the model simulation determined in stage 4, Figure 1.11 demonstrates that decreasing the proximal presynaptic inter-spike-interval (ISI) from 125 ms to 100 ms (a −20% change) or increasing the distal presynaptic ISI from 25 ms to 35 ms (a −40% change) results in a poorer match to the empirically observed ECD (> 10% change). While it is hard to say how the nonlinear nature of the HNN model

might affect gain changes associated with more drastic modifications to the input timing ISIs, this study assumes that a local minimum of the average RMSE cost function has been reached in the stage 4 simulation.

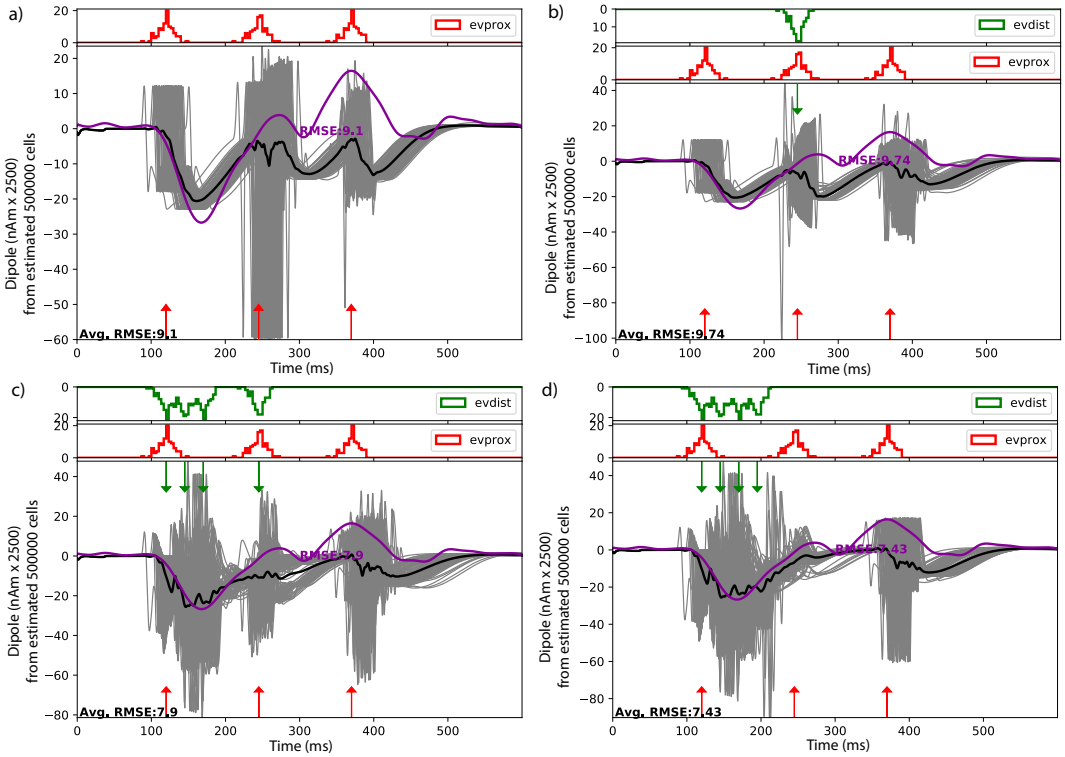

Figure 1.10. Simulations of the Aδ-N1 complex at four stages. All simulations are conducted with 100 trials (grey) to form the trial average (black) and compared via root mean squared error (RMSE) to the experimentally observed ECD (purple). Proximal (red) and distal (green) inputs are assigned successively as follows: a) add three proximal inputs at t = 120, 145, and 170 ms; b) add one distal input at t = 145 ms; c) add a three-spike burst of distal inputs 25 ms apart, starting at t = 120 ms; and d) adjust the last distal input to occur earlier at t = 195 ms. The top plots denote time histograms corresponding to each input. Note that the same local network and cellular parameters determined for the modeled Aβ-N20 complex ECD are used here.

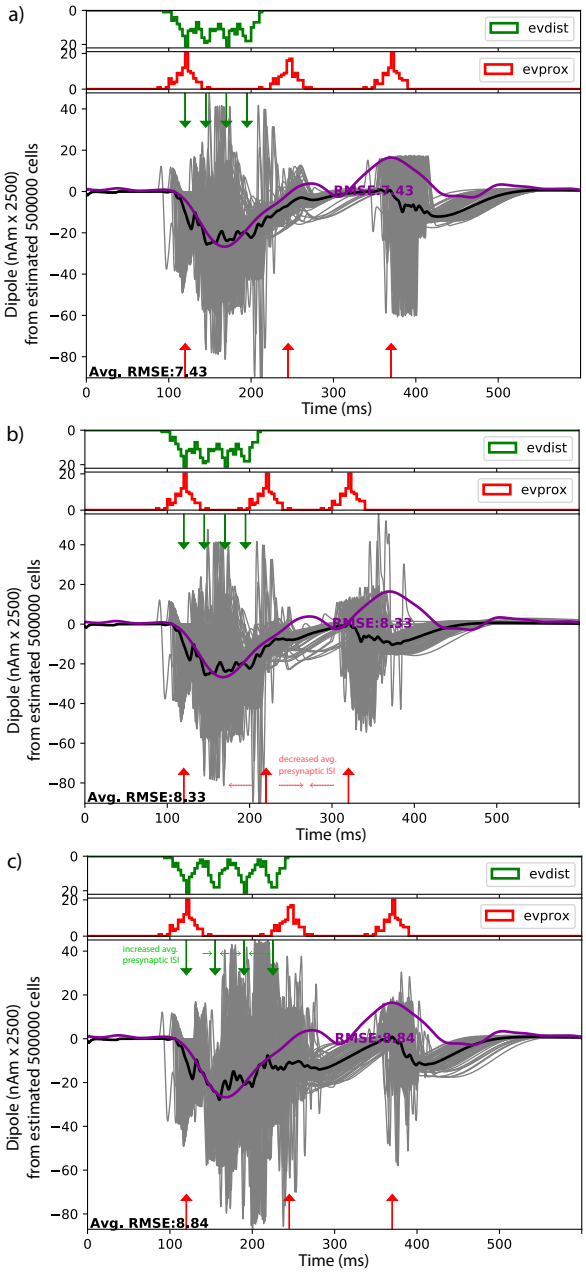

Figure 1.11. Decreased Aδ-N1 complex matching due to deviations in the input timing at stage 4. Starting off at the model simulation shown in stage 4 (Figure 1.10.d) (a), decreasing the proximal presynaptic ISI from 125 ms to 100 ms renders an average RMSE of 8.33 (b). On the other hand, increasing the distal presynaptic ISI from 25 ms to 35 ms renders an average RMSE of 8.84 (c).

1.3 Discussion

HNN modeling of the Aβ-N20 complex demonstrated that non-nociceptive early-latency MNEP, emerges from a distinctly successive proximal versus distal drive process. In

keeping with the traditional understanding of the mechanisms governing this response (Figure 1.12) [31, 32, 35, 45, 46], the initial N20 deflection is produced by proximal "feedforward" drive to the granular layer. Contrary to traditional understanding, however, is the requirement for a successive distal input at t = 32 ms post-stimulus. In particular, the HNN model failed to produce a large enough P35 deflect and successive N45 deflection when the distal input was excluded. While this is an interesting finding in and of itself, such a result would need in vivo laminar validation confirming that there is, indeed, a large current sink measured in the supragranular layers around t = 32 ms and that such a sink is the product of reliable, precisely-timed distal drive from either high-order cortex or non-lemniscal thalamus.

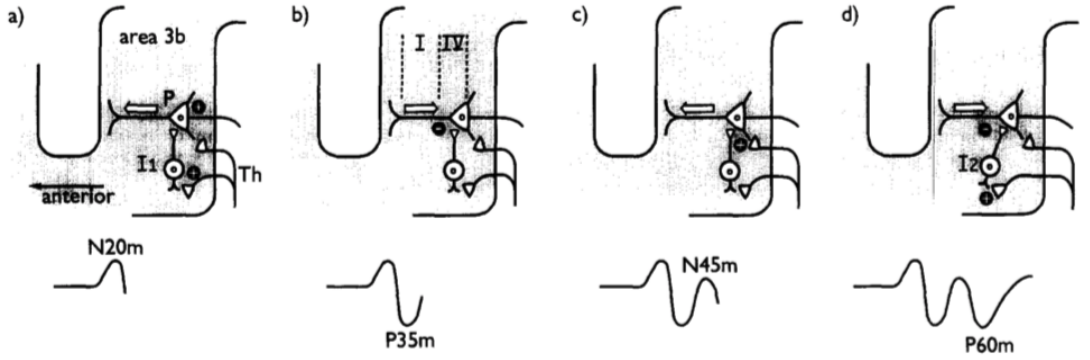

Figure 1.12. Traditional understanding of the circuit mechanisms behind the MNEP: a) excitatory drive from lemniscal thalamus enters the granular layer of area 3b, resulting in an initial depolarizing current being driven up the distal dendrites from the soma of the pyramidal cells, b) after a small time delay, inhibitory drive from activated basket cells reaches the pyramidal cell's soma, causing a net downward flow of current, a secondary excitatory drive excites the soma of the pyramidal cells and once again drive current up the distal dendrites, and d) secondary activation of the basket cells results in more inhibitory drive to the soma of pyramidal cells, resulting in another downward net current. Reproduced from Wikstrom et al. (1996), Fig. 6 [35].

For the Aδ-N1 complex, the HNN model provides a convincing account of the initial N1 downward deflection (lasting 125 ms), however, the circuit appears to be unable to adequately reproduce subsequent deflections in the waveform. At stage 1 (Figure 1.10a), the basic structure of the waveform is caused by activation of the L5 basket cells which supply heavy amounts of inhibition to the soma of L5 pyramidal via $GABA_B$

neurotransmitters. Since activation of $GABA_B$ receptors is associated with a notably long decay constant, a net hyperpolarizing current dominates the L5 pyramidal cell for a long time, driving current down the distal dendrites. The other proximal inputs play a similar role, though are spaced 125 ms apart in order to allow for upward deflections at t = 275 and 375 ms. Adding distal inputs in the following stages provide excitability to the pyramidal somas, allowing the system to recuperate more quickly from hyperpolarization.

Interestingly, the simulated dipole scaling factor for the Aδ-N1 complex (2500) was significantly larger than for the Aβ-N20 complex (30). This implies that the ECD of the Aδ-N1 complex was formed by an estimated 500,000 versus 6,000 cells and might indicate that the Aβ-N20 complex is significantly more spread out in area 3b of S1 (i.e., fewer single-neuron dipoles have a common normal component to the surface of the brain). The experimental observation that median nerve stimulation activates various populations in area 3b differently might explain why the Aβ-N20 complex is so robust yet of reduced magnitude [30, 33–35].

Noting that the presynaptic inter-spike-interval is ∼25 ms, the distal drive in (c) and (d) of Figure 1.10 indicates a 40 Hz gamma burst. While interpretation of a supposed "gamma" burst is open ended, some have argued that gamma might regulate a synchronous feedforward process that grades with nociceptive stimulus intensity rather than perception [47]. Such a notion is also supported by the observation that the Aδ-N1 complex appears to mediate motor over perceptual or autonomic responses [30]. Proximal drive occurring every ∼25 ms, on the other hand, indicates an 8 Hz theta (or low alpha) burst. Since theta is a well-known correlate of chronic pain and is often found to up-regulate in chronic pain subjects, nociception ascending to S1 might involve the same thalamocortical loop regulated by the reticular thalamic nucleus [47–49].

It is not hard to see that none of the mechanisms associated with the Aδ-N1 complex are in themselves unique. As presented by Mouraux and Iannetti (2009), LEPs can at times be explained by other sources of sensory input [50]. Thus, nociceptive somatosensory activity may not be entirely encoded by the Aδ-N1 complex.

Hypothesis 1 asserted that neural circuits producing the Aδ-N1 complex and Aβ-N20 complex ECDs were functionally congruent, and Hypothesis 2 extended Hypothesis 1 by predicting that the number and timing of proximal versus distal inputs could

account for the difference between the two waveform complexes. Therefore, tuning and simulating the HNN model under both hypotheses rendered a few key predictions for further inquiry:

1. The Aδ-N1 complex emerges from coinciding bursts of proximal and distal drive, phase locked to burst onset.

2. The proximal burst occurs with a 125 ms ISI (i.e., an 8 Hz theta frequency), and the distal burst occurs with a 25 ms ISI (i.e., a 40 Hz gamma frequency).

Future work should test these predictions via laminar S1 recordings in an animal model and experimental paradigm that isolates activation of the Aδ and Aβ fibers, respectively. We expect the initial evoked response following Aδ activation to differentiate from Aβ activation in that the former arrives significantly later (consistent with the Aδ fiber conduction velocity) and with two coinciding bursts to the granular and supragranular layers. These bursts should be of a high-theta/low-alpha and gamma frequency, respectively, with appropriate correction for the shift in frequency bands for the specific animal model. Furthermore, we expect laminar multi-unit activity to support the spiking associated with the HNN Aδ-N1 complex model at stage 4.

Part 2

Spectral event analysis in resting-state chronic pain EEG

2.1 Background

Lumbar radiculopathy (LR) is a well-documented source of chronic pain and is common in patients with failed back surgery syndrome [5, 51]. Despite its prevalence, LR and other sources of chronic pain remain particularly difficult to treat given our limited understanding of the cortical mechanisms governing perception of non-evoked, "spontaneous" pain. Numerous research groups have demonstrated signatures of both evoked [52–55] and chronic [18–20] pain in the frequency domain, however, these signatures lack a unified understanding that translates to both evoked and non-evoked pain.

In order to address the limitations of previous analysis methods, Part 2 of this study begins by asserting that all neural states have a beginning and end point. A cortical 40 Hz gamma oscillation, for instance, can arise at the onset of an inhibition-excitation interaction between pyramidal cells and fast-spiking interneurons [56, 57]. The circuit mechanisms that govern such a rhythm's creation or demise thus rely on precisely timed activation of various brain structures and their smaller, neuron-level components. Despite their simple underpinnings, other classes of supposedly oscillatory activity turn out to be far from constant rhythms [16]. For instance, reduced beta (14-29 Hz) activity associated with attention and detection tasks turns out to be better characterized as a reduction in beta *event* (defined as a transient peak in the time-frequency domain with high beta power relative to the median power spectral density)

probability rather than reduced oscillation amplitude [17, 43]. Yet, the probability of beta event occurrence has profound implications on cognitive processes given its propensity to modulate bottom-up saliency. Given our interest in the pain matrix, Part 2 of this study identifies bursts of rhythmic activity to inform the building blocks of the larger pain-encoding system. Most importantly, Part 2 considers resting state chronic pain activity without averaging out transient, spontaneous processes significant to the chronic pain brain state. To do this, we begin by characterizing each single-epoch, time-frequency response by its fluctuation from median power spectral density (PSD). This allows us to 1) identify frequency bands that exhibit temporal fluctuations containing large amounts of high-power events compared to that of healthy controls and 2) detect individual high-power events on a single-time-series basis. Once spectral events of a frequency band of interest are found, their respective features in the time-frequency domain (i.e., count/epoch, peak power, frequency-width, and time-width) can be measured for comparison between the two groups.

2.2 Materials and Methods

2.2.1 Human EEG trials

This experiment measured resting-state EEG for 42 human subjects. 20 subjects had a diagnosis of lumbar radiculopathy (LR), 20 were age and sex-matched healthy controls ($\pm$3 years), and 2 were healthy controls without an age match. Note that for the purpose of the present analysis, only trials from age-matched subjects were included in analysis. All subjects were screened for pre-diagnosed psychological disorders, were not taking opioid medication, could read and write English, and were instructed to abstain from coffee two hours prior to recordings. Furthermore, each LR subject reported a pain score of at least 5 on the 0-10 visual analog scale, while healthy controls reported a score of 0 at the time of recording. EEG recordings were collected using the Stat-Net/MicroEEG system with 16 electrodes (placed according to the International 10/20 system), a common reference positioned halfway between Fz and Cz, and a ground. All recording sessions were sampled at 250 Hz for a duration of 5 minutes each, beginning with the subject's eyes open and alternating between eyes open and eyes closed every 60 seconds. Each subject was seated comfortably in a quiet, secluded room and instructed

to relax.

2.2.2 Preprocessing and epoch selection

First, all electrode channels for each subject were visually inspected and marked for excessive amplitude or noise due to poor electrode connection. Since the channels corresponding to electrodes C3, CZ, F8, FP1, and FP2 passed visual inspection for all subjects, further analysis was restricted to these channels to maximize use of the sampled population. Raw EEG signals were then high-pass filtered at 1 Hz (1-1.5 Hz transition band, 80 dB stop band attenuation), low-pass filtered at 124 Hz (120-124 Hz transition band, 60 dB stop band attenuation), and notch filtered from 57-63 Hz (55-57 Hz and 63-65 Hz transition bands, 100dB stop band attenuation) using forward-reverse FIR filters. Following filtering, segments from each time series were binned according to their corresponding eyes open/closed condition. To account for artifacts, each 1-second bin of a given segment was tested against a validated support vector machine artifact detection classifier [58] and marked for rejection when positive. Among the artifact-free bins belonging to a segment, adjacent bin pairs were selected as single epochs for analysis. Given our need to characterize average resting state activity among presumably stochastic epochs, any subject along with its age-matched pair were discarded if less than 10 epochs (of a given combination of subject, condition, and channel) survived artifact detection. Thus, for the eyes open condition, subjects 8, 16, 18, 22, 27, 28, 31, 38, and 39 were omitted from analysis. For the eyes closed condition, only subjects 16 and 28 were omitted (due to lack of an age-matched, LR counterpart).

The time-frequency response (TFR) was calculated for each epoch by convolving in the time domain with a Morlet wavelet (width = 5) for frequencies ranging from 1-50 Hz. Spectrograms were cropped to eliminate edge effects, leaving each spectrogram to span 6-50 Hz in the frequency domain and 0-1072 ms in the time domain.

2.2.3 Identifying frequency bands of interest

All analysis was conducted for each combination of the selected channel and eyes open/closed condition separately. In keeping with the approach set forth by Shin et al. (2017), spectral events were characterized by first normalizing each TFR spectrogram by the median power spectral density (PSD), calculated across all epochs of a subject, eyes open/closed

condition, and channel combination) [17, 59]. With the understanding that spectral events define topographic regions in the time-frequency domain of highest factors-of-the-median (FOM) power, we subsequently sought to find frequency bands where the bulk level of transient spectral activity diverged between the LR and healthy groups. The procedure for identification of frequency bands of interest was conducted as follows:

1. Compute the average subject-specific TFR (averaged across epochs).
2. Compute the average subject-specific PSD.
3. At each frequency value, perform a two-tailed Wilcoxon rank sum test (tested at $\alpha = 0.05$ significance following Bonferroni correction for multiple comparisons) comparing the distribution of RL subject-specific PSD values to that of the healthy groups.

2.2.4 Spectral event detection and feature comparison

Given that the above procedure identified a band of interest for only one channel, C3, spectral event detection was conducted at 42-43 Hz for C3, eyes open epochs, and 38-43 Hz for C3, eyes closed epochs. This portion of the analysis used the SpectralEvents toolbox (https://github.com/jonescompneurolab/SpectralEvents) which characterized four event features: count/epoch, peak power, frequency-width (F-span), and time-width as in Shin et al. (2017) [17]. Note, however, that here we implemented an alternative event-finding method (`findMethod=3`), that does not allow for overlapping events to occur in a given suprathreshold region. Furthermore, it ensures that any within-band, suprathreshold activity will register an event. The procedure was as follows:

1. Threshold the normalized, single-epoch TFR (at 6 FOM) in the frequency band of interest.
2. Find local maxima.
3. Discard maxima of lesser magnitude in each suprathreshold region, respectively, such that only the greatest local maximum in each region survives. All preserved maxima (i.e., that are now separated into unique suprathreshold regions) characterize the center locations corresponding to each event in the time-series.

4. Define event counts/epoch as the number of events in the given epoch.

5. Define event power as the FOM value at the maxima (i.e., event center) for a given event.

6. Define event duration as the full-width at half-maximum along the time dimension for a given event.

7. Define event F-span as the full-width at half-maximum along the frequency dimension for a given event.

8. If more than one local maxima in a region have the same greatest value, their respective event timing, frequency location, and boundaries at full-width half-maximum are calculated separately and averaged.

Figure 2.1 shows event locations in time-frequency space for ten epochs associated with a LR subject.

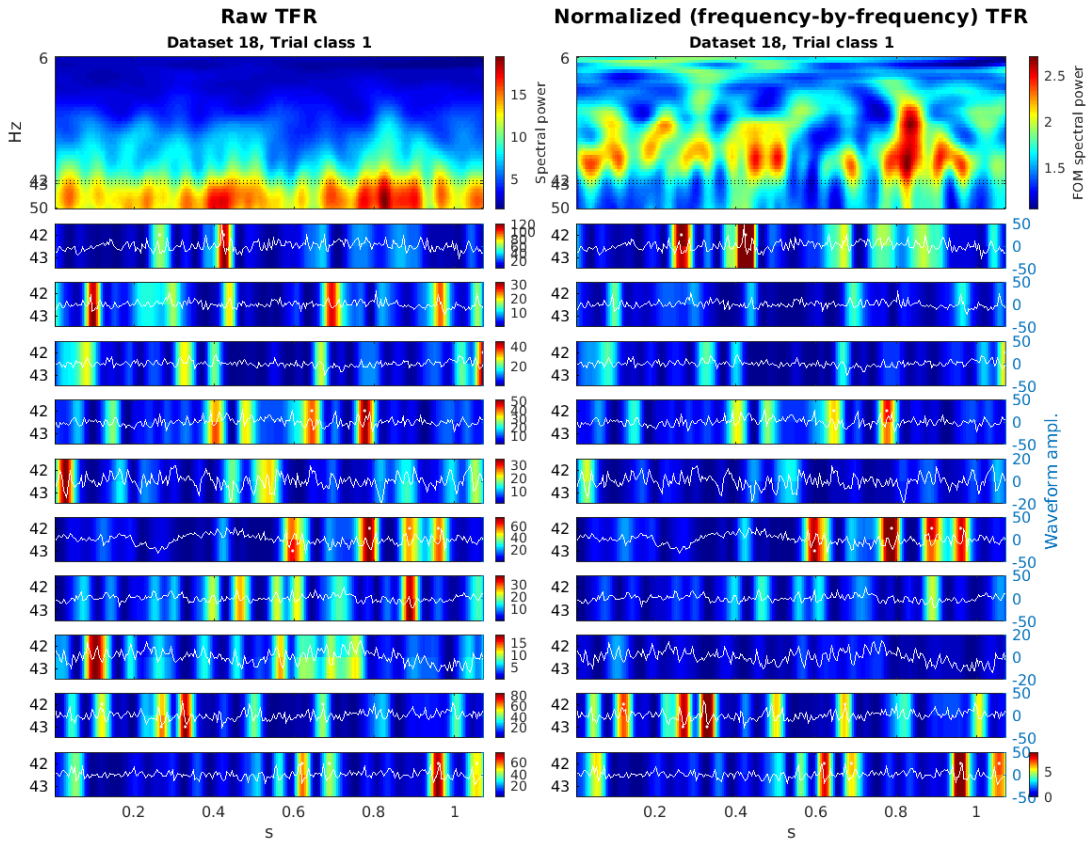

Figure 2.1. Spectral event detection in ten sample epochs for the 18th LR subject, eyes open. The top spectrogram displays the average TFR over all epochs. The ten bottom spectrograms display randomly sampled, single-epoch TFRs with their corresponding waveforms. Note that the ten bottom spectrograms only show activity in the frequency band of interest (42-43 Hz) and the left and right sides show the same TFR before and after median-PSD normalization, respectively. White dots correspond to the time-frequency coordinates of isolated spectral events calculated from the median-normalized TFR.

Once the spectral events were labeled and characterized, probability histograms were constructed for each feature. A two-tailed Wilcoxon rank sum tests was performed (at $\alpha = 0.01$ significance, following Bonferroni correction for multiple comparisons) for each feature, comparing the aggregate probability histogram between the LR and healthy groups.

2.3 Results

2.3.1 Only one frequency band near 40 Hz and over somatosensory cortex separates spontaneous EEG activity in LR versus healthy subjects

Only one electrode channel (C3, over the left somatosensory cortex) of five contains a frequency band that significantly diverged in normalized spectral activity between the LR and healthy groups. Figure 2.2 and Figure 2.3 demonstrate this result for the eyes open condition, and Figure 2.4 and Figure 2.5 demonstrate this for the eyes closed condition. Interestingly, the statistically significant frequency band is very similar in C3 for both the eyes open (42-43 Hz) and eyes closed (38-43 Hz) cases.

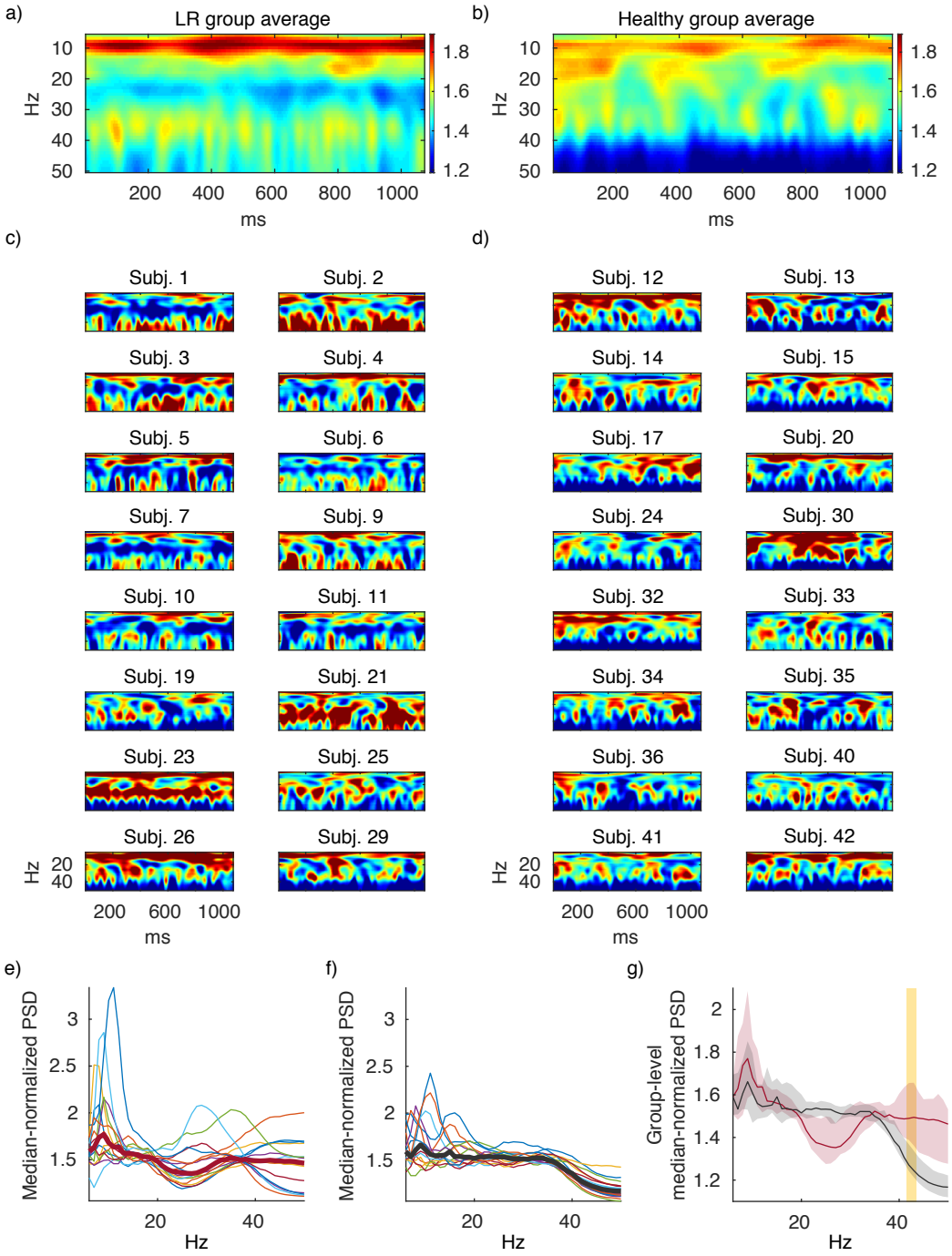

Figure 2.2. Characteristic median-normalized time-frequency domain activity for channel C3 (eyes open), compared between the LR versus healthy groups. The group average (a-b) is averaged across all subject-specific average TFRs (c-d). In (e-g), maroon corresponds with the LR group median and black corresponds with the healthy group median. In (g), the orange region (42-43 Hz) indicates statistically significant PSD differences between the two groups (two-tailed Wilcoxon rank sum test corrected for multiple comparisons at 0.05 significance, $p < 0.0011$). Confidence intervals are computed using a 10,000 iteration bootstrap procedure.

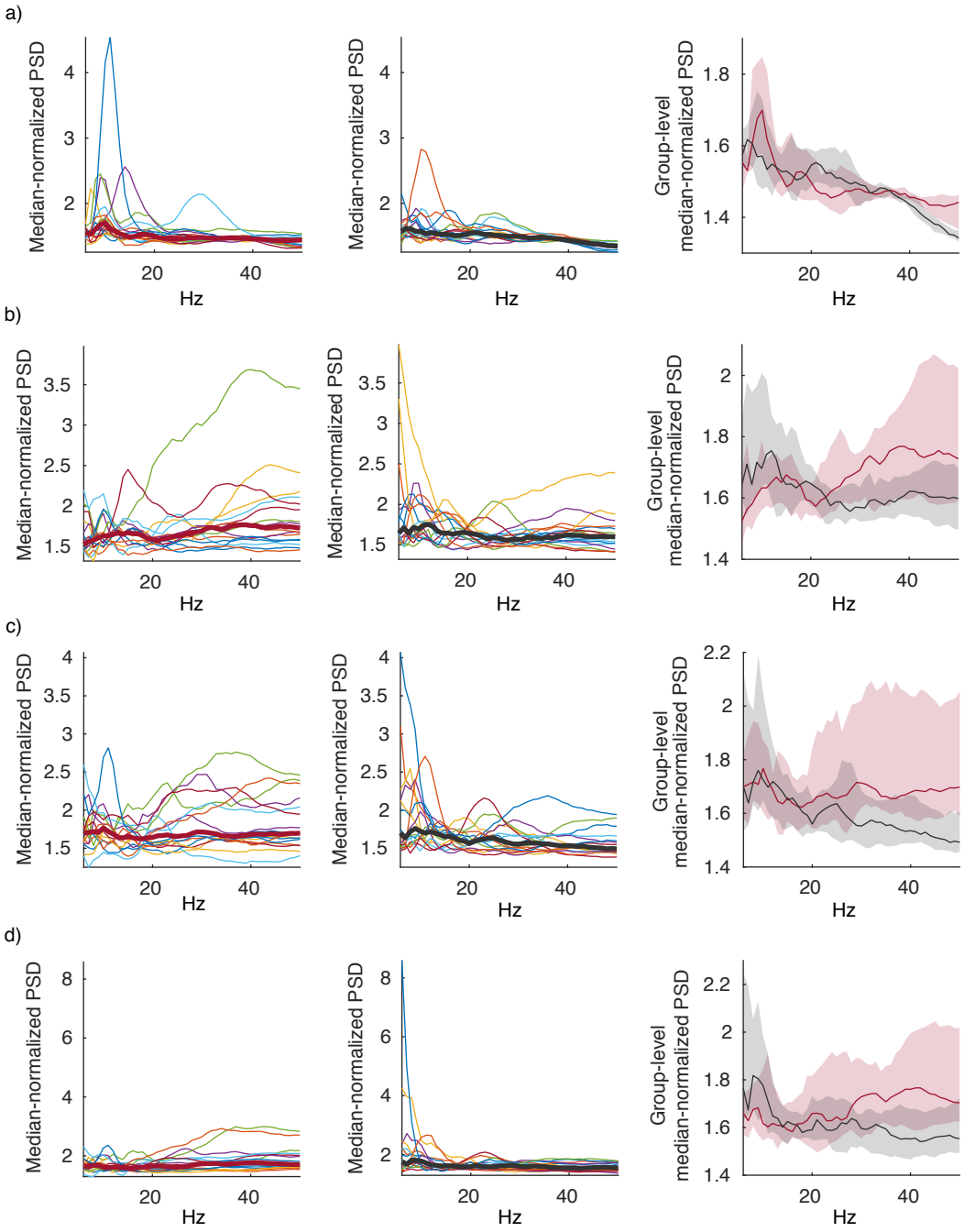

Figure 2.3. Median-normalized PSDs for all channels besides C3 (eyes open), compared between the LR versus healthy groups. Maroon corresponds with the LR group median and black corresponds with the healthy group median. No frequency values for channels CZ (a), F8 (b), FP1 (c), and FP2 (d) contain statistically significant PSD differences between the two groups (two-tailed Wilcoxon rank sum test corrected for multiple comparisons at 0.05 significance, $p > 0.0011$). Confidence intervals are computed using a 10,000 iteration bootstrap procedure.

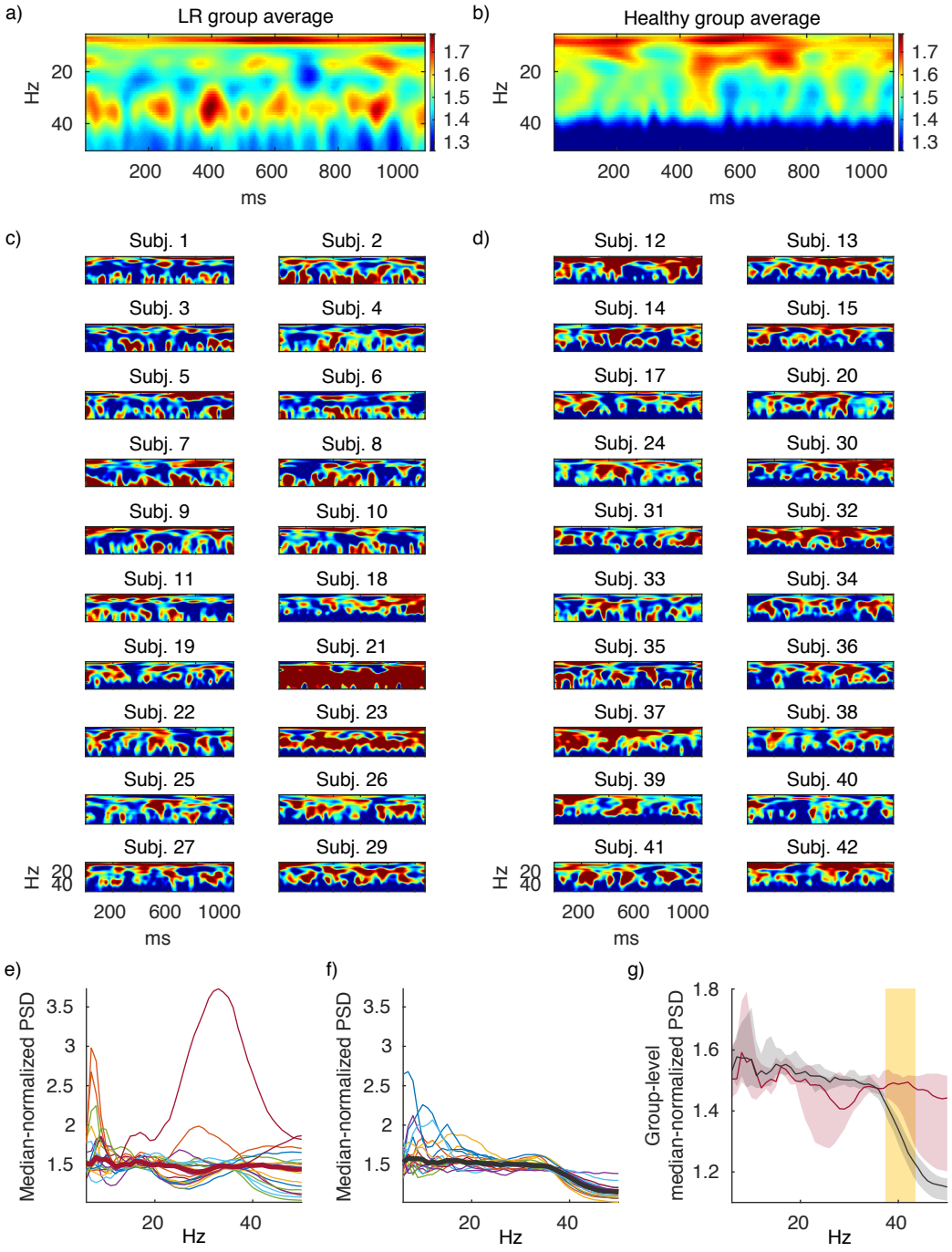

Figure 2.4. Characteristic median-normalized time-frequency domain activity for channel C3 (eyes closed), compared between the LR versus healthy groups. The group average (a-b) is averaged across all subject-specific average TFRs (c-d). In (e-g), maroon corresponds with the LR group median and black corresponds with the healthy group median. In (g), the orange region (38-43 Hz) indicates statistically significant PSD differences between the two group (Wilcoxon rank sum test corrected for multiple comparisons at 0.05 significance, $p < 0.0011$). Confidence intervals are computed using a 10,000 iteration bootstrap procedure.

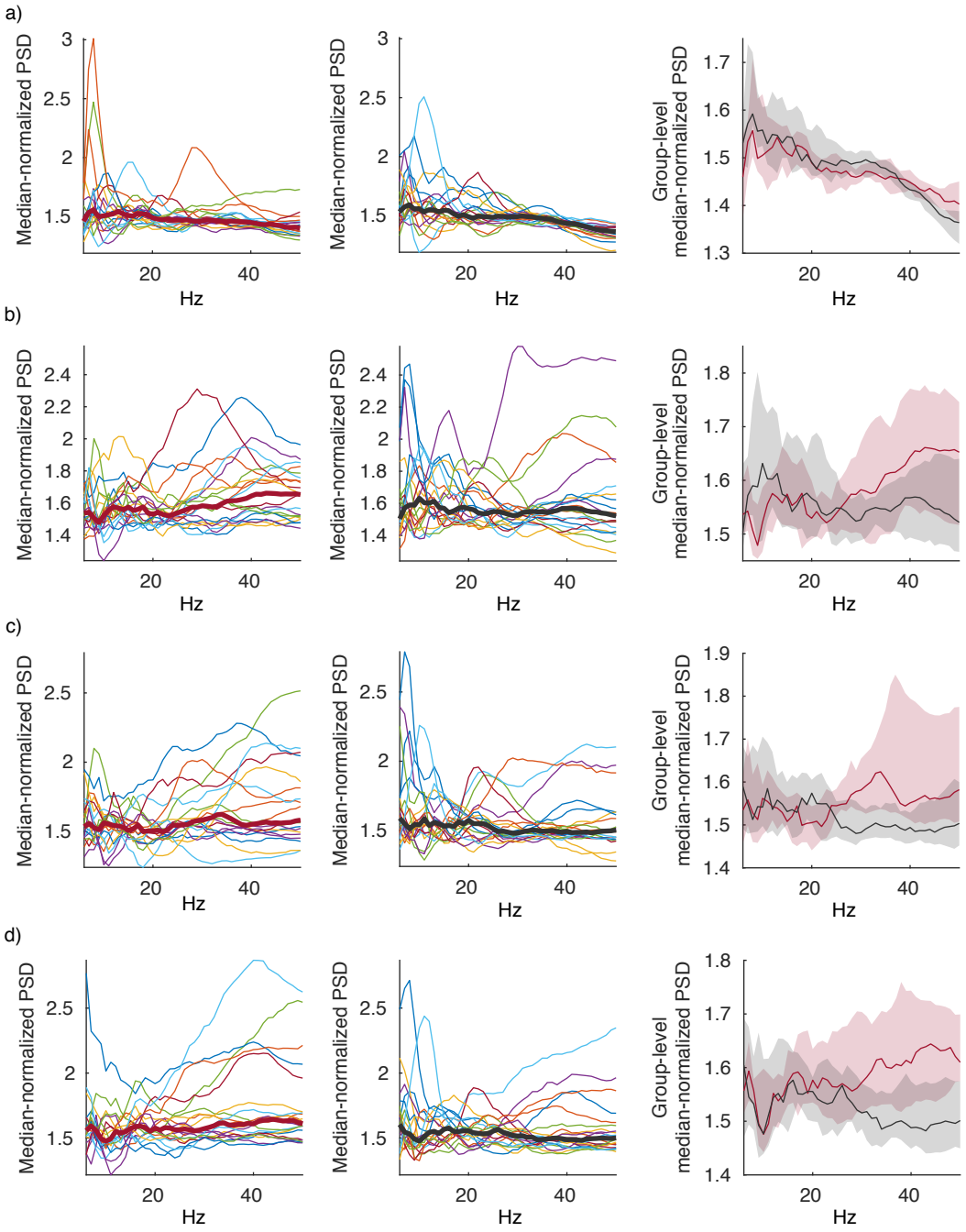

Figure 2.5. Median-normalized PSDs for all channels besides C3 (eyes closed), compared between the LR versus healthy groups. Maroon corresponds with the LR group median and black corresponds with the healthy group median. No frequency values for channels CZ (a), F8 (b), FP1 (c), and FP2 (d) contain statistically significant PSD differences between the two groups (Wilcoxon rank sum test corrected for multiple comparisons at 0.05 significance, $p > 0.0011$). Confidence intervals are computed using a 10,000 iteration bootstrap procedure.

2.3.2 The LR group exhibits 40 Hz spectral events at a different rate and with a different frequency-span compared to the healthy group

For the eyes open condition, 42-43 Hz spectral event analysis demonstrates that the feature distributions of counts/epoch (i.e., event rate), power, and event F-span are significantly different between the LR and healthy groups (Figure 2.6). For the eyes closed condition, 38-43 Hz spectral event analysis demonstrates that only event counts/epoch and F-span are significantly different between the LR and healthy groups (Figure 2.7). Therefore, event rate and F-span differentiate between the LR and healthy groups regardless of the eyes open/closed experimental condition.

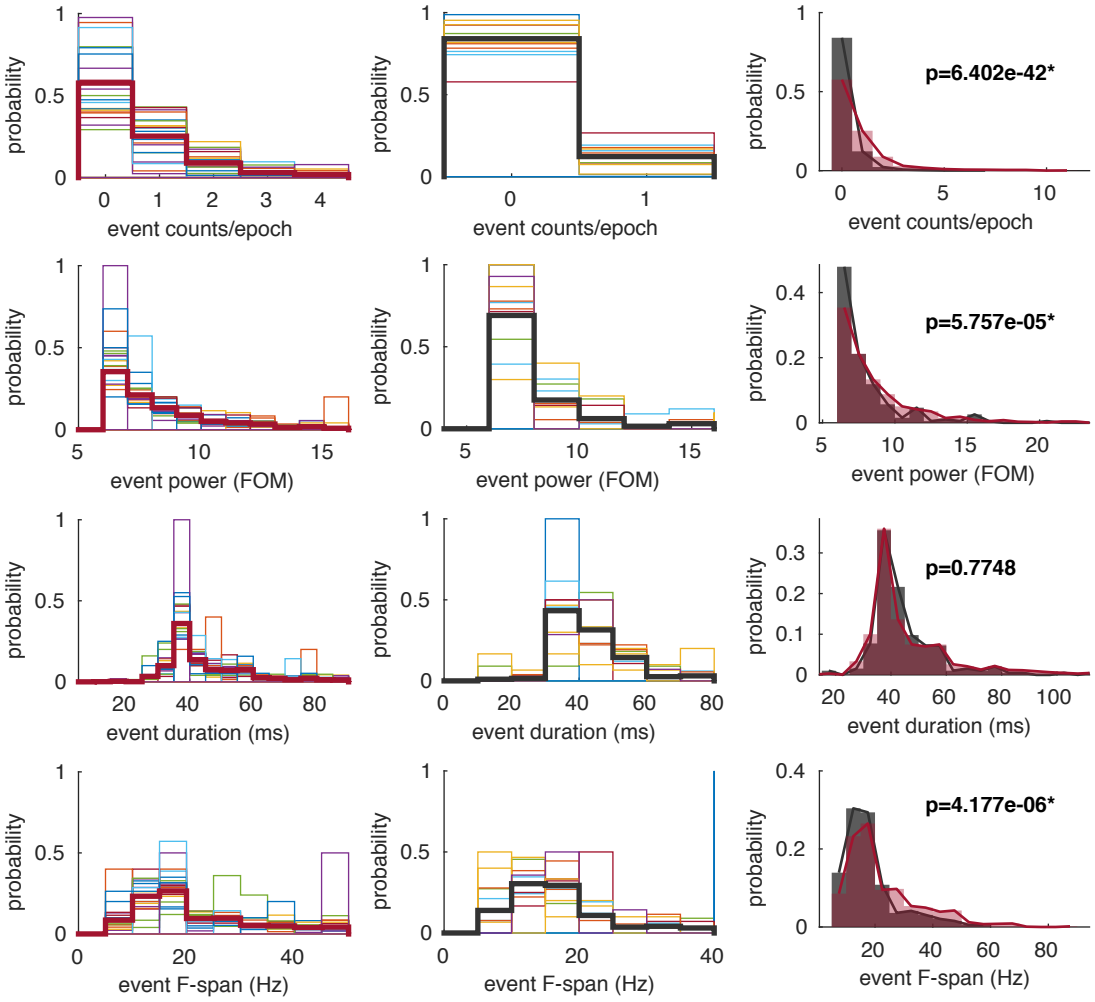

Figure 2.6. Probability histograms of spectral event features (counts/epoch, power, duration, and frequency span) in the 42-43 Hz range for channel C3, eyes open. From left to right: LR subjects, healthy controls, and subject aggregates from the respective groups. Maroon denotes the aggregate histogram for LR and black denotes the aggregate histogram for healthy subjects. *statistically significant difference between the aggregate feature distribution of the LR group compared to the healthy group (Wilcoxon rank sum test corrected for multiple comparisons at 0.01 significance, $p < 0.0025$).

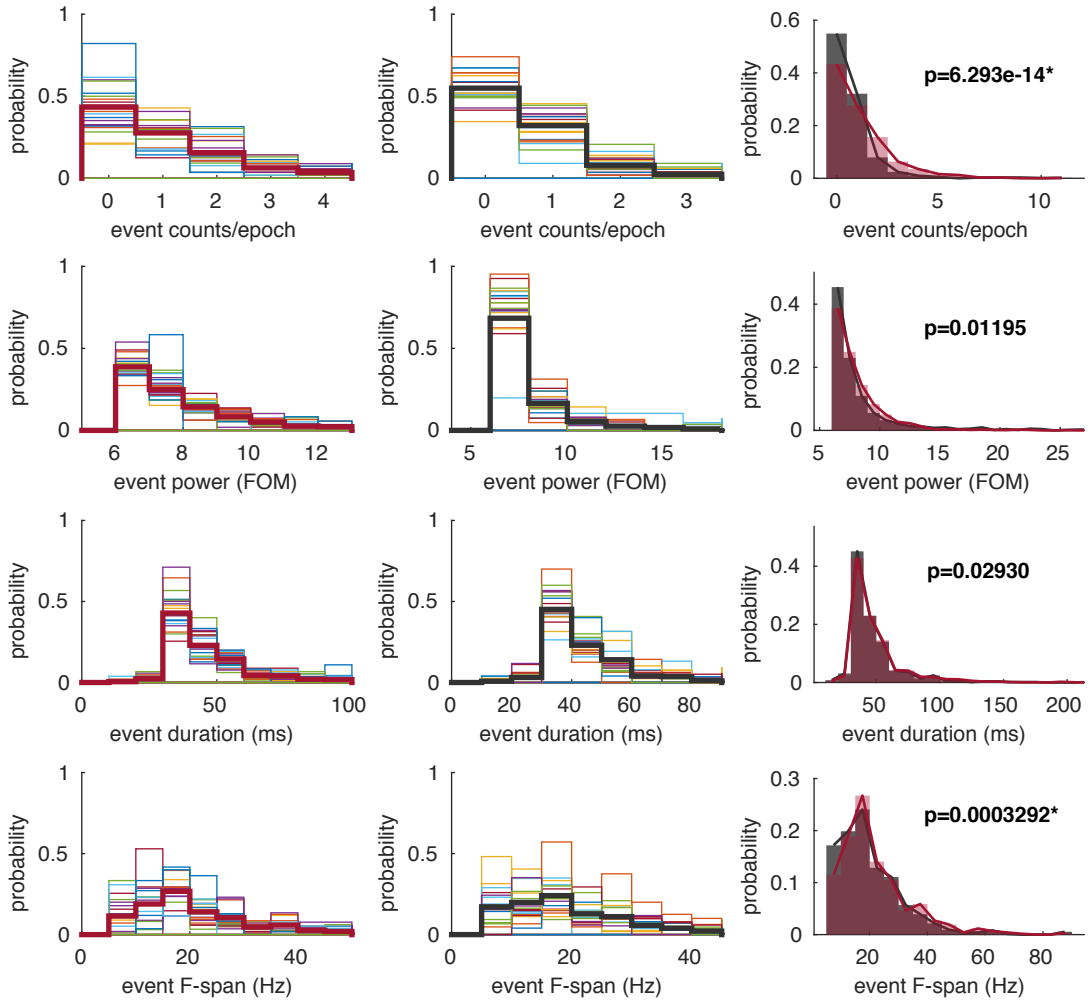

Figure 2.7. Probability histograms of spectral event features (counts/epoch, power, duration, and frequency span) in the 38-43 Hz range for channel C3, eyes closed. From left to right: LR subjects, healthy controls, and subject aggregates from the respective groups. Maroon denotes the aggregate histogram for LR subjects and black denotes the aggregate histogram for healthy subjects. *statistically significant difference between the aggregate feature distribution of the LR group compared to the healthy group (Wilcoxon rank sum test corrected for multiple comparisons at 0.01 significance, $p < 0.0025$).

2.4 Discussion

The first finding of Part 2 of this study demonstrates that only one frequency band (40.5 ± 2.5 Hz) differs significantly in spectral fluctuation between the LR and healthy groups. Such activity emerges from the C3 electrode over the somatosensory cortex

and is roughly conserved across the eyes open and eyes closed experimental conditions. While there is a slight difference in the boundaries of the isolated frequency bands between the eyes open (42-43 Hz) and eyes closed (38-43 Hz) conditions, its statistical significance remains to be determined in a subsequent study. Second, the separation between prominent high-power spectral fluctuations of the two groups corresponds to a statistically significant difference in spectral events. The observed aggregate distributions of spectral event counts/epoch (eyes open and eyes closed), power (eyes open), and frequency span (eyes open and eyes closed) differ between the LR group compared to the healthy group, while event duration does not.

The extent of chronic pain's causal influence on gamma spectral events (or vice versa) remains unknown, however, the increase in event counts/epoch points toward a more nuanced underlying mechanism. First, Figure 2.2 and Figure 2.4 show a notable (however statistically insignificant) downward deflection in the median-normalized beta band for LR subjects experiencing chronic pain. Conservative correction for multiple comparisons may have falsely rejected a band of beta activity containing downregulated beta events correlating with chronic pain symptoms. Therefore, increased gamma events at approximately 40 Hz could easily be the result of some intermediate process that upregulates feedforward (bottom-up) drive via rumination. Rumination—a state of focused awareness of pain—might produce an attentive state that downregulates beta events (associated with mediation from high-order cortex [60, 61] or non-lemniscal thalamus) in favor of ascending drive from lemniscal thalamic pathways [43]. When ascending projections from lemniscal thalamus dominate, excitation/inhibition interactions that create bursts of 40 Hz activity are more likely to emerge given the increased direct activation of parvalbumin interneurons [56, 57]. Further deactivation of lateral inhibition via thalamocortical dysrhythmia also creates irregular formation of random gamma events and is a widely observed phenomenon associated with chronic pain [18, 47, 49, 62, 63]. Evidence from previous studies also demonstrates that a downregulation of spontaneous beta events should result in a higher contribution of low alpha (8-14 Hz) in time-averaged spectral activity [22, 43, 64]. Gating of feedforward activity through the regulation of beta events thus accounts for the experimentally observed lower-frequency shift in dominant alpha peak power associated with prolonged pain sensitivity in numerous cortical regions [55, 65].

On one hand, the gamma spectral events observed in this study might be the result of heightened perceptual attention rather than pain, specifically. Conversely, it could be that a heightened state of perceptual attention helps define the chronic pain "brain state" by forcing saliency corresponding to a targeted somatotopic region. Such a mechanism might explain pain's ability to selectively modulate an individual's perceptual experience and provide considerable context dependency.

Another particularly intriguing feature of the results occurred in the variability of the PSD plots shown in Figure 2.2, Figure 2.3, Figure 2.4, and Figure 2.5. The amount of inter-subject variability contained in the median-normalized PSD traces among LR subjects exceeded that of the healthy subjects. By visual inspection, this trend is most noticible in channel C3—the channel with a statistically significant frequency band of interest. Interestingly, Li et al. (2018) shows that the for evoked fast-pain perception, inter-stimulus variability increased with pain rating [66]. While the circuit mechanisms underlying chronic and evoked pain are vastly different, EEG variability in response to increased pain sensitivity might be a conserved process.

Since statistical tests in this study were conducted on the observed distributions of aggregate features across subjects, bias from a small subset of subjects may have influenced comparisons between the LR and healthy groups. It should also be noted that we used a small sample size (n=16 for eyes open and n=20 for eyes closed) to approximate population-level effects in LR compared to healthy human subjects. To reduce such bias, future work should address the inter-subject variability of spectral event features in a larger number of subjects ($n > 100$ for each category).

Conclusion

This study examined a microcosm of dynamics in the pain matrix by isolating millisecond-scale events in the neocortex with circuit-level significance. While Part 1 specifically targeted S1, Part 2 considered activity originating from five electrodes where the only electrode exhibiting significant spectral event activity (C3) was located over S1 in the left hemisphere. For transmission of ascending nociceptive information, "events" are inputs to the equivalent current dipole responsible for an evoked response. For resting state, spontaneous pain, "events" are blips in spectral power that become visible only in the single-epoch time-frequency domain. Taken together, Part 1 and Part 2 make experimental predictions that call for validation in animal models as well as (for Part 2) implementation in a pain classifier that attempts to measure the usefulness of gamma spectral event features for separating chronic pain subjects from healthy subjects. Lastly, the methods of both parts outline a novel approach for addressing the circuit mechanisms underlying cortical pain processing.

References

1. Lenoir, C., Huang, G., Vandermeeren, Y., Hatem, S. M. & Mouraux, A. Human primary somatosensory cortex is differentially involved in vibrotaction and nociception. *Journal of Neurophysiology* **118,** 317–330 (2017).

2. Jin, Q., Wu, G., Peng, W., Xia, X., Hu, L. & Iannetti, G. Somatotopic representation of second pain in the primary somatosensory cortex of humans and rodents. *Journal of Neuroscience* **38,** 5538–5550 (2018).

3. Nahin, R. L. Estimates of pain prevalence and severity in adults: United States, 2012. *The Journal of Pain* **16,** 769–780 (2015).

4. Cameron, T. Safety and efficacy of spinal cord stimulation for the treatment of chronic pain: a 20-year literature review. *Journal of Neurosurgery: Spine* **100,** 254–267 (2004).

5. Kumar, K., Taylor, R. S., Jacques, L., Eldabe, S., Meglio, M., Molet, J., Thomson, S., O'callaghan, J., Eisenberg, E., Milbouw, G., *et al.* Spinal cord stimulation versus conventional medical management for neuropathic pain: a multicentre randomised controlled trial in patients with failed back surgery syndrome. *Pain* **132,** 179–188 (2007).

6. Saab, C. Y. Pain-related changes in the brain: diagnostic and therapeutic potentials. *Trends in Neurosciences* **35,** 629–637 (2012).

7. Mouraux, A. & Iannetti, G. D. The search for pain biomarkers in the human brain. *Brain* **141,** 3290–3307 (2018).

8. Tracey, I., Woolf, C. J. & Andrews, N. A. Composite Pain Biomarker Signatures for Objective Assessment and Effective Treatment. *Neuron* **101,** 783–800 (2019).

9. Treede, R.-D., Kenshalo, D. R., Gracely, R. H. & Jones, A. K. The cortical representation of pain. *Pain* **79,** 105–111 (1999).

10. Tracey, I. Nociceptive processing in the human brain. *Current Opinion in Neurobiology* **15,** 478–487 (2005).

11. Moisset, X. & Bouhassira, D. Brain imaging of neuropathic pain. *Neuroimage* **37,** S80–S88 (2007).

12. Melzack, R. From the gate to the neuromatrix. *Pain* **82,** S121–S126 (1999).

13. Tracey, I. & Mantyh, P. W. The cerebral signature for pain perception and its modulation. *Neuron* **55,** 377–391 (2007).

14. Mouraux, A., Diukova, A., Lee, M. C., Wise, R. G. & Iannetti, G. D. A multisensory investigation of the functional significance of the "pain matrix". *NeuroImage* **54,** 2237–2249 (2011).

15. Moulton, E. A., Elman, I., Pendse, G., Schmahmann, J., Becerra, L. & Borsook, D. Aversion-related circuitry in the cerebellum: responses to noxious heat and unpleasant images. *Journal of Neuroscience* **31,** 3795–3804 (2011).

16. Jones, S. R. When brain rhythms aren't 'rhythmic': implication for their mechanisms and meaning. *Current Opinion in Neurobiology* **40,** 72–80 (2016).

17. Shin, H., Law, R., Tsutsui, S., Moore, C. I. & Jones, S. R. The rate of transient beta frequency events predicts behavior across tasks and species. *eLife* **6,** e29086 (2017).

18. Sarnthein, J., Stern, J., Aufenberg, C., Rousson, V. & Jeanmonod, D. Increased EEG power and slowed dominant frequency in patients with neurogenic pain. *Brain* **129,** 55–64 (2005).

19. Vuckovic, A., Gallardo, V. J. F., Jarjees, M., Fraser, M. & Purcell, M. Prediction of central neuropathic pain in spinal cord injury based on EEG classifier. *Clinical Neurophysiology* **129,** 1605–1617 (2018).

20. Kim, J. A., Bosma, R. L., Hemington, K. S., Rogachov, A., Osborne, N. R., Cheng, J. C., Oh, J., Crawley, A. P., Dunkley, B. T. & Davis, K. D. Neuropathic pain and pain interference are linked to alpha-band slowing and reduced beta-band

magnetoencephalography activity within the dynamic pain connectome in patients with multiple sclerosis. *Pain* **160,** 187–197 (2019).

21. Jones, S. R., Pritchett, D. L., Stufflebeam, S. M., Hämäläinen, M. & Moore, C. I. Neural correlates of tactile detection: a combined magnetoencephalography and biophysically based computational modeling study. *Journal of Neuroscience* **27,** 10751–10764 (2007).

22. Jones, S. R., Pritchett, D. L., Sikora, M. A., Stufflebeam, S. M., Hamalainen, M. & Moore, C. I. Quantitative analysis and biophysically realistic neural modeling of the MEG mu rhythm: rhythmogenesis and modulation of sensory evoked responses. *Journal of Neurophysiology* (2009).

23. Neymotin, S., Daniels, D., Peled, N., McDougal, R., Carnevale, N., Moore, C., Hines, M., Hamalainen, M. & Jones, S. *Human Neocortical Neurosolver (2018)* doi:DOI10.5281/zenodo.1446517.

24. Timmermann, L., Ploner, M., Haucke, K., Schmitz, F., Baltissen, R. & Schnitzler, A. Differential coding of pain intensity in the human primary and secondary somatosensory cortex. *Journal of Neurophysiology* **86,** 1499–1503 (2001).

25. Ploner, M., Schmitz, F., Freund, H.-J. & Schnitzler, A. Parallel activation of primary and secondary somatosensory cortices in human pain processing. *Journal of Neurophysiology* **81,** 3100–3104 (1999).

26. Whitsel, B., Favorov, O., Li, Y., Lee, J., Quibrera, P. & Tommerdahl, M. Nociceptive afferent activity alters the SI RA neuron response to mechanical skin stimulation. *Cerebral Cortex* **20,** 2900–2915 (2010).

27. Vierck, C. J., Whitsel, B. L., Favorov, O. V., Brown, A. W. & Tommerdahl, M. Role of primary somatosensory cortex in the coding of pain. *Pain* **154,** 334–344 (2013).

28. Kenshalo, D. R., Iwata, K., Sholas, M. & Thomas, D. A. Response properties and organization of nociceptive neurons in area 1 of monkey primary somatosensory cortex. *Journal of Neurophysiology* **84,** 719–729 (2000).

29. Kanno, A., Nakasato, N., Hatanaka, K. & Yoshimoto, T. Ipsilateral area 3b responses to median nerve somatosensory stimulation. *NeuroImage* **18,** 169–177 (2003).

30. Tiihonen, J., Hari, R. & Hämäläinen, M. Early deflections of cerebral magnetic responses to median nerve stimulation. *Electroencephalography and Clinical Neurophysiology* **74,** 290–296 (1989).

31. Cauller, L. J. & Kulics, A. The neural basis of the behaviorally relevant N1 component of the somatosensory-evoked potential in SI cortex of awake monkeys: evidence that backward cortical projections signal conscious touch sensation. *Experimental Brain Research* **84,** 607–619 (1991).

32. Lipton, M. L., Fu, K.-M. G., Branch, C. A. & Schroeder, C. E. Ipsilateral hand input to area 3b revealed by converging hemodynamic and electrophysiological analyses in macaque monkeys. *Journal of Neuroscience* **26,** 180–185 (2006).

33. Lin, Y.-Y., Chen, W.-T., Liao, K.-K., Yeh, T.-C., Wu, Z.-A., Ho, L.-T. & Lee, L.-S. Differential generators for N20m and P35m responses to median nerve stimulation. *NeuroImage* **25,** 1090–1099 (2005).

34. Huttunen, J., Komssi, S. & Lauronen, L. Spatial dynamics of population activities at S1 after median and ulnar nerve stimulation revisited: an MEG study. *NeuroImage* **32,** 1024–1031 (2006).

35. Wikström, H., Huttunen, J., Korvenoja, A., Virtanen, J., Salonen, O., Aronen, H. & Ilmoniemi, R. Effects of interstimulus interval on somatosensory evoked magnetic fields (SEFs): a hypothesis concerning SEF generation at the primary sensorimotor cortex. *Electroencephalography and Clinical Neurophysiology* **100,** 479–487 (1996).

36. Lin, Y.-Y., Shih, Y.-H., Chen, J.-T., Hsieh, J.-C., Yeh, T.-C., Liao, K.-K., Kao, C.-D., Lin, K.-P., Wu, Z.-A. & Ho, L.-T. Differential effects of stimulus intensity on peripheral and neuromagnetic cortical responses to median nerve stimulation. *NeuroImage* **20,** 909–917 (2003).

37. Schroeder, C., Seto, S., Arezzo, J. C. & Garraghty, P. Electrophysiological evidence for overlapping dominant and latent inputs to somatosensory cortex in squirrel monkeys. *Journal of Neurophysiology* **74,** 722–732 (1995).

38. Burke, D., Mackenzie, R., Skuse, N. & Lethlean, A. Cutaneous afferent activity in median and radial nerve fascicles: a microelectrode study. *Journal of Neurology, Neurosurgery & Psychiatry* **38,** 855–864 (1975).

39. Chen, J.-R., Wang, Y.-J. & Tseng, G.-F. The effect of epidural compression on cerebral cortex: a rat model. *Journal of Neurotrauma* **20,** 767–780 (2003).

40. Gramfort, A., Luessi, M., Larson, E., Engemann, D., Strohmeier, D., Brodbeck, C., Goj, R., Jas, M., Brooks, T., Parkkonen, L. & Hämäläinen, M. MEG and EEG data analysis with MNE-Python. *Frontiers in Neuroscience* **7,** 267 (2013).

41. Gramfort, A., Luessi, M., Larson, E., Engemann, D. A., Strohmeier, D., Brodbeck, C., Parkkonen, L. & Hämäläinen, M. S. MNE software for processing MEG and EEG data. *NeuroImage* **86,** 446–460 (2014).

42. Jaeger, D. & Jung, R. *Encyclopedia of Computational Neuroscience* (Springer Publishing Company, Incorporated, 2015).

43. Sherman, M. A., Lee, S., Law, R., Haegens, S., Thorn, C. A., Hämäläinen, M. S., Moore, C. I. & Jones, S. R. Neural mechanisms of transient neocortical beta rhythms: converging evidence from humans, computational modeling, monkeys, and mice. *Proceedings of the National Academy of Sciences* **113,** E4885–E4894 (2016).

44. Hämäläinen, M., Hari, R., Ilmoniemi, R. J., Knuutila, J. & Lounasmaa, O. V. Magnetoencephalography—theory, instrumentation, and applications to noninvasive studies of the working human brain. *Reviews of Modern Physics* **65,** 413 (1993).

45. Peterson, N. N., Schroeder, C. E. & Arezzo, J. C. Neural generators of early cortical somatosensory evoked potentials in the awake monkey. *Electroencephalography and Clinical Neurophysiology* **96,** 248–260 (1995).

46. Ikeda, H., Wang, Y. & Okada, Y. C. Origins of the somatic N20 and high-frequency oscillations evoked by trigeminal stimulation in the piglets. *Clinical Neurophysiology* **116,** 827–841 (2005).

47. Ploner, M., Sorg, C. & Gross, J. Brain rhythms of pain. *Trends in Cognitive Sciences* **21,** 100–110 (2017).

48. LeBlanc, B. W., Cross, B., Smith, K. A., Roach, C., Xia, J., Chao, Y.-C., Levitt, J., Koyama, S., Moore, C. I. & Saab, C. Y. Thalamic bursts down-regulate cortical theta and nociceptive behavior. *Scientific Reports* **7,** 2482 (2017).

49. Vanneste, S., Song, J.-J. & De Ridder, D. Thalamocortical dysrhythmia detected by machine learning. *Nature Communications* **9,** 1103 (2018).

50. Mouraux, A. & Iannetti, G. D. Nociceptive laser-evoked brain potentials do not reflect nociceptive-specific neural activity. *Journal of Neurophysiology* (2009).

51. Yamashita, T., Kanaya, K., Sekine, M., Takebayashi, T., Kawaguchi, S. & Katahira, G. A quantitative analysis of sensory function in lumbar radiculopathy using current perception threshold testing. *Spine* **27,** 1567–1570 (2002).

52. Li, X., Zhao, Z., Ma, J., Cui, S., Yi, M., Guo, H. & Wan, Y. Extracting neural oscillation signatures of laser-induced nociception in pain-related regions in rats. *Frontiers in Neural Circuits* **11,** 71 (2017).

53. Peng, W., Xia, X., Yi, M., Huang, G., Zhang, Z., Iannetti, G. & Hu, L. Brain oscillations reflecting pain-related behavior in freely moving rats. *Pain* **159,** 106 (2018).

54. Tiemann, L., Hohn, V. D., Dinh, S. T., May, E. S., Nickel, M. M., Gross, J. & Ploner, M. Distinct patterns of brain activity mediate perceptual and motor and autonomic responses to noxious stimuli. *Nature communications* **9,** 4487 (2018).

55. Furman, A. J., Meeker, T. J., Rietschel, J. C., Yoo, S., Muthulingam, J., Prokhorenko, M., Keaser, M. L., Goodman, R. N., Mazaheri, A. & Seminowicz, D. A. Cerebral peak alpha frequency predicts individual differences in pain sensitivity. *NeuroImage* **167,** 203–210 (2018).

56. Cardin, J. A., Carlén, M., Meletis, K., Knoblich, U., Zhang, F., Deisseroth, K., Tsai, L.-H. & Moore, C. I. Driving fast-spiking cells induces gamma rhythm and controls sensory responses. *Nature* **459,** 663 (2009).

57. Sohal, V. S., Zhang, F., Yizhar, O. & Deisseroth, K. Parvalbumin neurons and gamma rhythms enhance cortical circuit performance. *Nature* **459,** 698 (2009).

58. Levitt, J., Nitenson, A., Koyama, S., Heijmans, L., Curry, J., Ross, J. T., Kamerling, S. & Saab, C. Y. Automated detection of electroencephalography artifacts in human, rodent and canine subjects using machine learning. *Journal of Neuroscience Methods* **307,** 53–59 (2018).

59. Feingold, J., Gibson, D. J., DePasquale, B. & Graybiel, A. M. Bursts of beta oscillation differentiate postperformance activity in the striatum and motor cortex of monkeys performing movement tasks. *Proceedings of the National Academy of Sciences* **112,** 13687–13692 (2015).

60. Womelsdorf, T., Ardid, S., Everling, S. & Valiante, T. A. Burst firing synchronizes prefrontal and anterior cingulate cortex during attentional control. *Current Biology* **24,** 2613–2621 (2014).

61. Bressler, S. L. & Richter, C. G. Interareal oscillatory synchronization in top-down neocortical processing. *Current opinion in neurobiology* **31,** 62–66 (2015).

62. Llinás, R. R., Ribary, U., Jeanmonod, D., Kronberg, E. & Mitra, P. P. Thalamocortical dysrhythmia: a neurological and neuropsychiatric syndrome characterized by magnetoencephalography. *Proceedings of the National Academy of Sciences* **96,** 15222–15227 (1999).

63. Llinás, R., Urbano, F. J., Leznik, E., Ramírez, R. R. & Van Marle, H. J. Rhythmic and dysrhythmic thalamocortical dynamics: GABA systems and the edge effect. *Trends in Neurosciences* **28,** 325–333 (2005).

64. Jones, S. R., Kerr, C. E., Wan, Q., Pritchett, D. L., Hämäläinen, M. & Moore, C. I. Cued spatial attention drives functionally relevant modulation of the mu rhythm in primary somatosensory cortex. *Journal of Neuroscience* **30,** 13760–13765 (2010).

65. Lim, M., Kim, J. S., Kim, D. J. & Chung, C. K. Increased low-and high-frequency oscillatory activity in the prefrontal cortex of fibromyalgia patients. *Frontiers in human neuroscience* **10,** 111 (2016).

66. Li, L., Huang, G., Lin, Q., Liu, J., Zhang, S. & Zhang, Z. Magnitude and Temporal Variability of Inter-stimulus EEG Modulate the Linear Relationship Between Laser-Evoked Potentials and Fast-Pain Perception. *Frontiers in Neuroscience* **12** (2018).